INTERNATIONAL JOURNAL FOR NUMERICAL METHODS IN ENGINEERING
Int. J. Numer. Meth. Engng 2012; **92**:238–267
Published online 9 June 2012 in Wiley Online Library (wileyonlinelibrary.com). DOI: 10.1002/nme.4335

An XFEM-based numerical strategy to model mechanical interactions between biological cells and a deformable substrate

Mehdi Farsad and Franck J. Vernerey*,†

Department of Civil, Environmental and Architectural Engineering, University of Colorado at Boulder, Campus Box 428, Boulder, CO 80309-0428, USA

SUMMARY

Contractile cells are known to constantly probe and respond to their mechanical environment through mechanosensing. Although the very mechanisms responsible for this behavior are still obscure, it is now clear that cells make full use of cross-talks between mechanics, chemistry, and transport to organize their structure and generate forces. To investigate these processes, it is important to derive mathematical and numerical models that can accurately capture the interactions between cells and an underlying deformable substrate. The present paper therefore introduces a computational framework, based on the extended FEM (XFEM) and the level set method, to model the evolution of two-dimensional (plane stress) cells lying on an elastic substrate whose properties can be varied. Cells are modeled with a continuum mixture approach previously developed by the authors to describe key phenomena of cell sensing, such as stress fiber formation, mechanosensitive contraction, and molecular transport whereas cell–substrate adhesion is formulated with a linear elastic cohesive model. From a numerical viewpoint, cell and substrate are discretized on a single, regular finite element mesh, whereas the potentially complex cell geometry is defined in terms of a level set function that is independent of discretization. Field discontinuities across the cell membrane are then naturally enforced using enriched shape functions traditionally used in the XFEM formulation. The resulting method provides a flexible platform that can handle complex cell geometries, can avoid expensive meshing techniques, and can potentially be extended to study cell growth and migration on an elastic substrate. In addition, the XFEM formalism facilitates the consideration of the cell's cortical elasticity, a feature that is known to be important during cell deformation. The proposed method is illustrated with a few biologically relevant examples of cell–substrate interactions. Generally, the method is able to capture some key phenomena observed in biological systems and displays numerical versatility and accuracy at a moderate computational cost. Copyright © 2012 John Wiley & Sons, Ltd.

Received 13 June 2011; Revised 19 November 2011; Accepted 13 March 2012

KEY WORDS: cell; substrate; contraction; XFEM; level set

1. INTRODUCTION

Tissue structure and dynamics are the result of intense mechanical cross-talks between contractile cells and their surrounding matrix, but the underlying mechanisms of such interactions are not understood yet. This has hindered critical research advances to translate tissue engineering to a wide variety of tissues, in which tissue development depends on mechanical forces, extracellular matrix properties, and initial specimen geometry [1]. A number of studies [2–4] have shown that the contraction of cells was responsible for the large deformations observed in artificial tissues soon after cell encapsulation. It was further found that these deformations were associated with significant changes in cell morphology and extracellular matrix structure and were strongly dependent on the mechanical environment of the tissue (such as tissue stiffness, stress, and deformation).

*Correspondence to: Franck J. Vernerey, Department of Civil, Environmental and Architectural Engineering, University of Colorado at Boulder, Campus Box 428, Boulder, CO 80309-0428, USA.

†E-mail: Franck.Vernerey@colorado.edu

This behavior is readily observed during the alignment of cells and collagen fibers in directions of maximum tensile stresses [5–7] and maximum effective stiffness. A key to understand these phenomena resides in our ability to characterize how cells interact with their environment and especially how they are able to sense their mechanical surrounding and react by producing contractile forces. Recent advances in cell mechanics, combined with latest developments in computational mechanics, may provide critical tools to study cell–matrix interactions. The objective of this paper is therefore to propose a numerical approach that can naturally describe how cells of arbitrary morphologies can sense the mechanical properties of their environment and respond to it by applying mechanical forces.

Mechanical models of cells can generally be split into two categories: formulations based on prestress fibrous network [8, 9] and those based on continuum mechanics [10, 11]. Because of their flexibility, continuum models have thus far been successful at capturing the chemomechanical interactions responsible for the mechanosensitivity of cells [12, 13]. For instance, mixture models have been proven to be very efficient at accurately characterizing certain key mechanisms of cell behavior, including transport, chemical reaction, and mass exchange [14]. In addition, the role of the cortical membrane surrounding the cell, known to be a critical player in cell deformation, has been the object of several modeling investigations. Models based on fibrous network mechanics have been the first to provide compelling arguments onto the role of membrane stiffness on cell curvature [9]. However, more recently, we have shown that continuum models can naturally incorporate the effect of cortex stiffness with a surface elasticity formulation based on the extended FEM (XFEM) [15]. The issue of modeling mechanical interactions between cells and a substrate has mostly been achieved via cohesive laws in finite element models [16–19]. Although successful at capturing interesting behaviors such as debonding, this strategy generally suffers from the fact that cell and substrate are defined on two distinct domains that typically exhibit complex geometries and possibly evolve in time. In many cases, such methods consequently lead to potential meshing issues and require a very fine discretization to reach accurate results.

To fill the gap, the present paper introduces a continuum formulation, combined with a numerical approach based on the XFEM and the level set approaches to study the mechanical crosstalks between contractile cells (fibroblasts) and a two-dimensional deformable substrate. The mechanochemistry of cell contraction is described in terms of a constrained mixture formulation that was recently developed by the authors [14] to capture the phenomena of mechanosensitive stress fiber (SF) formation (and dissociation) and contraction. In short, the model is based on the description of the contractile apparatus of cell in terms of two solid constituents, the cytoskeleton and a population of contractile SFs, as well as two fluid constituents, the cytosol and soluble contractile units (that can polymerize into SFs). The interactions between a cell and its substrate are possible through localized adhesive regions, known as the focal adhesion. From a numerical viewpoint, the complicated problem of the interactions between two domains (cell and substrate) of different geometry and constitution is greatly simplified by using the advantages of the XFEM [20–22]. Without loss of generality, considering cell and substrate as two-dimensional domains satisfying plane stress conditions, we introduce a single finite element mesh for both domains. Cell geometry is then defined in terms of an analytical level set function defining the contour of cell boundary independently of discretization. Degrees of freedom pertaining to cell are then only associated with nodes belonging to the interior of the domain defined by the level set, whereas discontinuities across the cell boundary are naturally represented by enriching finite element shape function with discontinuous functions following the standard XFEM equations. We show that this formulation has many advantages compared with standard finite element formulations. Although discussed more in details in the manuscript, the proposed framework provides a simple way to describe complex cell morphologies independently from discretization. This feature therefore circumvents potential meshing issues, especially when three-dimensional problems are considered. From a more practical viewpoint, the method is in line with recent experimental techniques relying on the level set method [23] to assess the evolution of cell population in time. This offers interesting possibilities for integrated experimental–numerical studies in which experimental imaging can directly be incorporated into a finite element simulation. Further, the attraction of the XFEM to describe the mechanical interaction between the relatively stiff cortical membrane surrounding the cell and its

DOI: 10.1002/nme

overall deformation has been addressed in a previous study [15]. We show here that this feature can be naturally coupled with a model for SF remodeling to capture realistic cell behaviors. At last, the level set method is ideal to model phenomena such as growth and evolution [24], which are inherent in cell spreading and remodeling. The present framework, although not addressing the problem of growth, is an important stepping stone to engaging in such study in the future.

The organization of the paper is as follows. In the next section, we give a summary of the constrained mixture model to characterize cell contraction; we particularly concentrate on providing the main equations (conservation of mass and momentum) as well as a set of biologically relevant assumptions to build realistic constitutive relations. In Section 3, the problem of the interaction between a cell and a deformable substrate is investigated. Governing equations are derived in both their strong and weak form, which enables a smooth transition to the finite element formulation presented in Section 4. Section 4 then discusses the XFEM–level set approach to obtain a solution of the cell–substrate interactions, leading to the final form of implicit, time-dependent finite element equations. The method is then illustrated in Section 5 by presenting several experimentally motivated example of cell–substrate interactions with comparison to observations. The paper finishes with a brief summary and concluding remarks.

2. A CONSTRAINED MIXTURE MODEL OF CONTRACTILE CELLS

2.1. Continuum description of cell's structure

The mechanosensing capability of cells is closely related to their contractile abilities. The latter has mainly been explained in terms of the formation of a well-differentiated network of SFs that are capable of generating forces through actomyosin interactions [14, 25, 26]. The main processes behind cell contraction can generally be decomposed as follows: first, the assembly of SF from dissolved contractile units and second, the contractile capacity of SFs. On the one hand, SF assembly and dissociation are known to be very sensitive to mechanical stimuli; mechanical force stabilizes existing SFs and promotes the assembly of new ones [26]. On the other hand, the contractile capacity of SFs is regulated by cross-bridge dynamics, which is known to be very sensitive to strain and strain rate. The evolution of SF therefore depends on the ability of cells to sense and transmit mechanical force from the substrate through so-called focal adhesion complexes (Figure 5) [27]. These complexes provide a physical attachment between SFs and substrate-anchoring molecules (ligands) through cross-membrane proteins (integrins) and may be thought of as cohesion islands of finite size between cell and substrate [28, 29]. At last, the internal structure of fibroblasts possesses sub-membranous mechanical reinforcement, known as the cortex, which is found in the form of a thin layer of actin fibers oriented in parallel with the membrane [9, 30–32]. This component is known to have a significant effect on the cell's morphology and deformation by providing a non-negligible tangential stiffness to the cell membrane [15].

From a modeling perspective, cell and substrate can be defined by two physical domains Ω^c and Ω^s in their current configuration, whose boundaries are denoted by Γ^c and Γ^s, respectively (Figure 1). Whereas a substrate is modeled as a purely elastic medium, a contractile cell is viewed

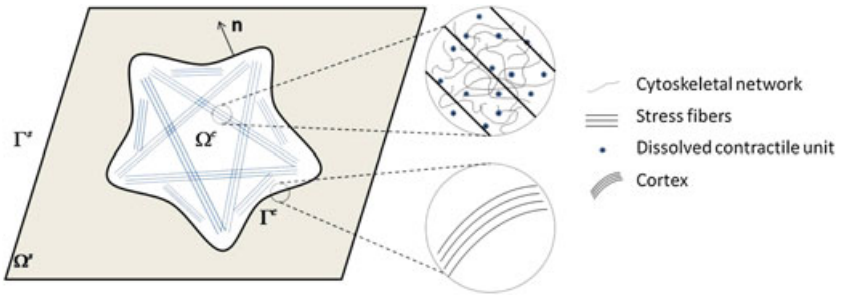

Figure 1. A typical cell on a substrate: the definition of domains and boundaries and a cell's main constituents.

DOI: 10.1002/nme

as a constrained mixture made of four constituents [14] (Figure 1): two solid constituents, a passive cytoskeleton (mostly made of microtubules and intermediate filaments) and a highly anisotropic SF network, and two fluid components, the cytosol and a population of dissolved contractile units. Measuring material motion with respect to the passive cytoskeleton, for which a point in the original configuration is denoted by $\mathbf{X}$, we can give a description of the mixture at any time t in terms of respective volume fraction ϕ^α of the diverse constituents. Considering a saturated mixture, it can further be shown that the summation of all volume fractions at a point is equal to 1, that is, $\sum_{\alpha=1}^{4} \phi^\alpha(\mathbf{X}, t) = 1$, where $\alpha = \mathrm{s, f, m, p}$ for passive cytoskeleton, cytosol, dissolved contractile units, and SFs, respectively. When placed on elastic substrates, fibroblasts usually evolve quickly in a configuration in which their thickness is significantly smaller than other dimensions, which motivates our study within the context of two-dimensional plane stress assumptions. This generally simplifies the analysis as SF directions only occupy the two-dimensional space and can be described in terms of one orientation angle. At any point within the cell, the SF network may then be defined in terms of the so-called structure tensor $\mathbf{\Phi}^{\mathrm{p}}$ given by [14]

$$\mathbf{\Phi}^{\mathrm{p}}(\mathbf{X}, t) = \phi^{\mathrm{p}} \left[\eta \mathbf{I} + (1 - 2\eta)\, \mathbf{M}_{\theta_0}\right], \qquad \mathbf{M}_{\theta_0} = \begin{bmatrix} \cos^2\theta_0 & \cos\theta_0 \sin\theta_0 \\ \cos\theta_0 \sin\theta_0 & \sin^2\theta_0 \end{bmatrix}, \tag{1}$$

providing a description of the anisotropic network in terms of its volume fraction ϕ^{p}, degree of anisotropy η, and principal orientation θ_0.

2.2. *Balance of mass and stress fiber evolution*

Let us first describe the mass balance of each constituent in a cell during the process of contraction. With the use of the material time derivative (following the solid constituent), the general form of mass balance equation for constituent α can be written as [14]

$$\frac{D\phi^{\mathrm{f}}}{Dt} + \phi^{f} \nabla \cdot \mathbf{v} + \nabla \cdot \mathbf{J}^{\mathrm{f}} = 0, \tag{2}$$

$$\frac{D\phi^{\mathrm{m}}}{Dt} + \phi^{m} \nabla \cdot \mathbf{v} + \nabla \cdot \mathbf{J}^{\mathrm{m}} = \Pi^{\mathrm{m}}, \tag{3}$$

where the solid velocity $\mathbf{v}$, the relative cytosol flux $\mathbf{J}^{\mathrm{f}}$, and the flux $\mathbf{J}^{\mathrm{m}}$ of unassembled contractile units (measured with respect to solid motion) are defined as follows:

$$\mathbf{v} = \frac{\partial \mathbf{x}(\mathbf{X}, t)}{\partial t}, \qquad \mathbf{J}^{\mathrm{f}} = \phi^{\mathrm{f}} \left(\mathbf{v}^{\mathrm{f}} - \mathbf{v}\right) \quad \text{and} \quad \mathbf{J}^{\mathrm{m}} = \phi^{\mathrm{m}} \left(\mathbf{v}^{\mathrm{m}} - \mathbf{v}\right). \tag{4}$$

The term Γ^{m} describes the rate of consumption (or production) of unassembled contractile units during their assembly into SFs. The mass and orientation of SFs therefore increase (or decrease) during time because of this chemical reaction. To describe this process, one may investigate the balance of mass of SFs in specific directions. We showed in [14] that this translates into a tensorial equation of the form

$$\frac{D\mathbf{\Phi}^{\mathrm{p}}}{Dt} + \mathbf{\Phi}^{\mathrm{p}} \nabla \cdot \mathbf{v} = \mathbf{\Pi}^{\mathrm{p}}, \tag{5}$$

where $\mathbf{\Pi}^{\mathrm{p}}$ is a second-order tensor that represents the directional rate of SF polymerization (or degradation). Importantly, it is assumed that once created, SF becomes part of the solid cytoskeleton and thus follows the same motion as the passive cytoskeleton. In other words, the velocity $\mathbf{v}^{\mathrm{p}}$ of the SF network is equal to the velocity $\mathbf{v}$ defined in (4). Finally, it is critical to specify that no mass can be created or consumed at the level of the entire mixture. This means that the change in mass of unassembled contractile units must be equal to the opposite of the change of mass of SFs at any location and time. This condition is written as follows:

$$\mathrm{trace}\,(\mathbf{\Pi}^{\mathrm{p}}) + \Pi^{\mathrm{m}} = 0. \tag{6}$$

DOI: 10.1002/nme

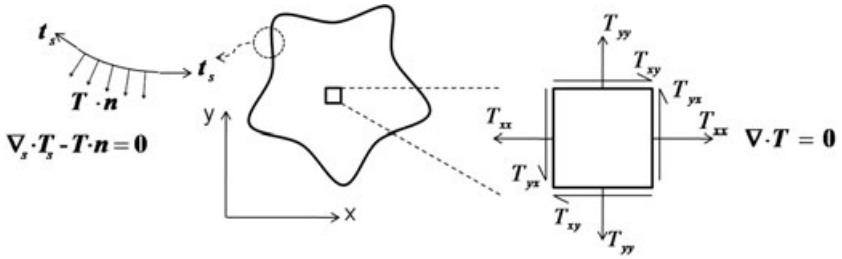

Figure 2. Equilibrium of forces in the body and the boundary of a cell.

2.3. Balance of momentum

Let us now turn to the governing equation describing the equilibrium of forces within a cell (Figure 2). For this, it is of interest to define the mixture Cauchy stress tensor $\mathbf{T}$ representing the infinitesimal force per unit current area. Using the effective stress principle, we can decompose the mixture stress into a contribution from each constituent,

$$\mathbf{T} = \mathbf{T}^{\mathrm{c}} + \mathbf{T}^{\mathrm{p}} - p\mathbf{I}, \tag{7}$$

where $\mathbf{T}^{\mathrm{c}}$ is the partial stress in the passive cytoskeleton, $\mathbf{T}^{\mathrm{p}}$ is the stress that originates from the presence of SFs, and p is the fluid pressure. Note that the contribution from the pressure of dissolved contractile proteins has been neglected because of its relatively low volume fraction. Considering the balance of momentum for the mixture, we can derive the form

$$\nabla \cdot \mathbf{T} + \mathbf{b} = \mathbf{0} \quad \text{in} \quad \Omega^{\mathrm{c}}, \tag{8}$$

representing the balance of force within the cell domain. Note that dynamical effects (through the inertial term) were neglected because of the slow processes into consideration. Finally, we note that by invoking the balance of angular momentum, we can show that stresses $\mathbf{T}^{\mathrm{c}}$, $\mathbf{T}^{\mathrm{p}}$, and $\mathbf{T}$ are represented symmetric tensors. Let us now investigate the effect of the cortical membrane stiffness on the equilibrium of force within the cell. Considering a small cortical thickness relative to the cell size, it is possible to represent force in the cortex in terms of a surface stress $\mathbf{T}_\sigma$ that has a unit of a force per unit length. As discussed in [15] and [9], one can show that the equilibrium between bulk stress $\mathbf{T}$ and membrane tensile stress $\mathbf{T}_\sigma$ is given by

$$\nabla_\sigma \cdot \mathbf{T}_\sigma - \mathbf{T} \cdot \mathbf{n} = 0 \quad \text{on} \quad \Gamma^{\mathrm{c}}, \tag{9}$$

where $\nabla_\sigma \cdot \mathbf{T}_\sigma$ denotes the surface divergence of the cortical stress and $\mathbf{n}$ is the outward normal vector to the cell's boundary Γ^{c}. A strong analogy may be drawn between the preceding equation and the Young–Laplace equation describing the effect of surface tension on the pressure in a fluid bubble. An increase in surface stress $\mathbf{T}_\sigma$ as well as membrane curvature (captured in the surface divergence operator) results in an increasing bulk stress in a direction normal to the membrane.

2.4. Fluid flux and cytoskeleton elasticity

Let us now discuss the constitutive relations describing cytosol and unassembled contractile units transport within the cell, as well as the passive elasticity of the passive cytoskeleton and its surrounding cortical membrane. The constitutive relation defining SF formation and contraction is left for the next section. The motion of the fluid phase is determined based on the following two assumptions. First, it is assumed that dissolved proteins are highly diluted and do not affect the motion of the cytosol. This means that one can describe cytosol motion uniquely in terms of the pressure gradient through Darcy's law as follows:

$$\mathbf{J}^{\mathrm{f}} = -\frac{\kappa}{\mu}\nabla p. \tag{10}$$

DOI: 10.1002/nme

Here, κ denotes the isotropic permeability of the cytoskeleton and μ is the viscosity of the cytosol. Note that because of the appearance of SF, the permeability may become anisotropic in time. This effect is not accounted for in the present study. In addition, we assume that the motion of dissolved proteins is driven by two forces: (1) the drag force of the cytosol and (2) the diffusive forces through the cytosol. One can therefore show that the flux $\mathbf{J}^{\mathrm{m}}$ of proteins contains a convection and diffusion term,

$$\mathbf{J}^{\mathrm{m}} = -\frac{\phi^{\mathrm{m}}}{\phi^{\mathrm{f}}}\frac{\kappa}{\mu}\nabla p - \phi^{\mathrm{f}} D\ \nabla\left(\frac{\phi^{\mathrm{m}}}{\phi^{\mathrm{f}}}\right), \tag{11}$$

where D is the diffusion coefficient of dissolved proteins in the cytosol.

To characterize the elasticity of the passive cytoskeleton, a hypo-elastic constitutive relation was adopted. With the introduction of the rate of deformation $\mathbf{D}(\mathbf{X}, t)$ of the solid constituent (Figure 3), an objective rate of Cauchy stress can be determined as follows:

$$\mathbf{T}^{\nabla J} = \mathbf{C}^{\nabla J} : \mathbf{D}, \quad \text{where} \quad \mathbf{D} = \frac{1}{2}\left(\frac{\partial \mathbf{v}}{\partial \mathbf{x}} + \frac{\partial \mathbf{v}^{\mathrm{T}}}{\partial \mathbf{x}}\right). \tag{12}$$

Assuming isotropic elasticity, the stiffness matrix $\mathbf{C}^{\nabla J}$ was expressed in terms of Lame constants λ and μ such that its components are given by $C^{\nabla J}_{ijkl} = 2\mu\delta_{ik}\delta_{jl} + \lambda\delta_{ij}\delta_{kl}$. Although the nonlinear material behavior of the passive cytoskeleton is not considered in the present formulation, nonlinear effects arising from finite deformation and rotation are still accounted for through the objective Jaumann rate of the Cauchy stress defined by

$$\mathbf{T}^{\nabla J} = \frac{D\mathbf{T}}{Dt} - \mathbf{W}\cdot\mathbf{T} - \mathbf{T}\cdot\mathbf{W}^{\mathrm{T}}, \tag{13}$$

where $\mathbf{W}$ denotes the spin tensor. For consistency, a similar hypo-elastic relation is also adopted to describe the effect of the cortical membrane. Thus, the Jaumann rate of the stress tensor $\mathbf{T}_\sigma$ is written in terms of the tangential velocity gradient on the cell boundary Γ^{c} as follows:

$$\mathbf{T}^{\sigma J}_{\sigma} = \mathbf{C}_\sigma : \mathbf{D}_\sigma, \quad \text{where} \quad \mathbf{D}_\sigma = \mathbf{P}\cdot\mathbf{D}\cdot\mathbf{P}. \tag{14}$$

Here, the tangential projection operator is given by $\mathbf{P} = \mathbf{I} - \mathbf{n}\otimes\mathbf{n}$. Note that for two-dimensional plane stress problems, the cortical membrane is represented by a line whose axial stiffness is given in terms of a single parameter E_σ. In this context, the components of the fourth-order cortical elasticity tensor $\mathbf{C}_\sigma$ is simply given by the following:

$$C_{\sigma,ijkl} = E_\sigma \delta_{ik}\delta_{jl}. \tag{15}$$

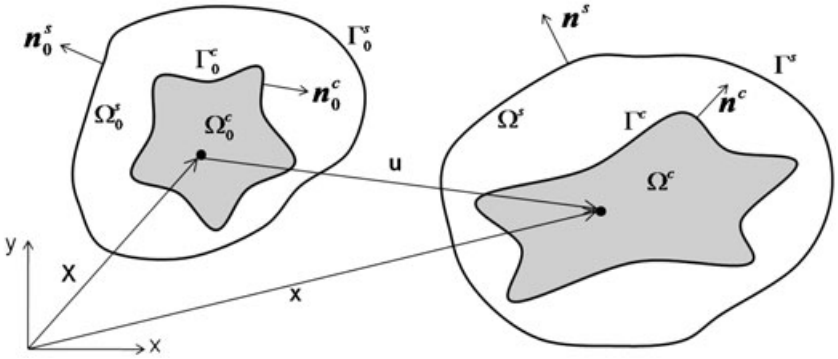

Figure 3. Initial and current configurations of cell and substrate domains.

DOI: 10.1002/nme

2.5. *Mechanosensitive stress fiber formation and contraction*

We now concentrate on the constitutive relation describing the active behavior of contractile cells, comprised of two distinct mechanisms: SF formation (or dissociation) and SF contraction. As mentioned previously, these processes are highly mechanosensitive, and the model should reflect such observations. Our formulation therefore builds upon the following two ideas:

- SF formation in a specific direction is promoted by the existence of a contractile stress in that particular direction. This assumption is supported by a variety of experimental observations such as those in [9, 25, 26, 33–36]. To capture this feature, we write the rate of SF formation $\mathbf{\Pi}^{\mathrm{p}}$ in terms of a first-order kinetic equation whose rate of formation is stress dependent:

$$\mathbf{\Pi}^{\mathrm{p}} = \underbrace{\left(\frac{1}{2}k_0^{\mathrm{f}}\mathbf{I} + k_1^{\mathrm{f}}\mathbf{T}^{\mathrm{p}}\right)\frac{\phi^{\mathrm{m}}}{\phi^{\mathrm{f}}}}_{\text{contraction-dependent formation}} - \underbrace{k_0^{\mathrm{d}}\mathbf{\Phi}^{\mathrm{p}}}_{\text{dissociation}}. \tag{16}$$

  Here, k_0^{f} and k_0^{d} are the tension-independent rate of formation and dissociation whereas k_1^{f} characterizes the sensitivity of formation to the level of contraction, represented by the tensor $\mathbf{T}^{\mathrm{p}}$. Note that the preceding equation is tensorial and is therefore capable of capturing direction-dependent SF formation and dissociation.
- SF contraction is dependent on the unidirectional strain and strain rate of SFs. This behavior is a well-known consequence of cross-bridge dynamics between thin and thick filaments at the molecular scale [37, 38]. In short, the model predicts a drop in contraction when the rate of shortening is negative and an increase in contraction with SF lengthening; this behavior is known as the tension–velocity relationship [38] and is represented by the normalized function g of strain rate $\dot{\epsilon}$ as follows (Figure 4):

$$g(\dot{\varepsilon}) = 1 + \frac{\dot{\varepsilon}/\dot{\varepsilon}_0}{\sqrt{(\dot{\varepsilon}/\dot{\varepsilon}_0)^2 + 1}}. \tag{17}$$

  In addition, the contraction magnitude is known to be optimal when SFs are in their original (strain-free) configuration. However, as they shorten or lengthen, their contractile capacity decreases to eventually vanish. This behavior, known as the length–tension relationship [37], is captured by introducing the function of uniaxial strain ϵ (Figure 4),

$$f(\varepsilon) = \exp\left(-\frac{\varepsilon}{\varepsilon_0}\right)^2 + H(\epsilon)\left(\frac{\varepsilon}{\varepsilon_1}\right)^2, \tag{18}$$

  where H is the Heaviside function such that $H = 0$ when $\epsilon < 0$ and $H = 1$ when $\epsilon \geqslant 0$. In the preceding equation, the first term captures the length–tension relation whereas the second term describes the nonlinear strain-hardening passive elastic response of SF when stretched. This term is important in capturing the increase in cell stiffness as more SFs are assembled. The stress tensor arising from the SF may then be determined by taking a directional average of

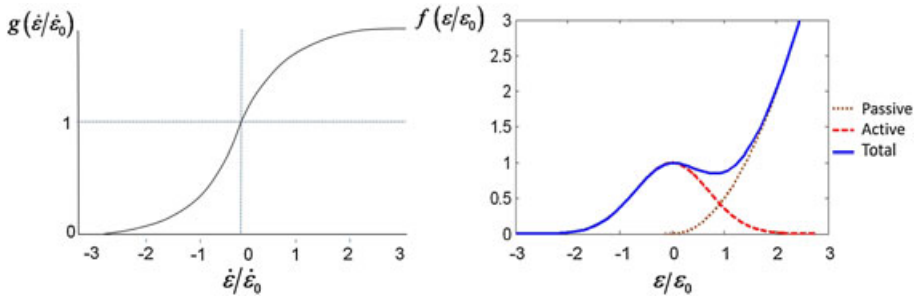

Figure 4. Tension of a single stress fiber as a function of strain and rate of strain.

DOI: 10.1002/nme

their contribution in each direction. Assuming that the normalized uniaxial stress in a specific direction is given by the product of functions g and f, weighted by their volume fraction ϕ^{p}, the stress $\mathbf{T}^{p}$ is defined by

$$\mathbf{T}^{\mathrm{p}} = \frac{\bar{T}}{\pi} \int_{-\pi/2}^{\pi/2} \phi^{\mathrm{p}}(\theta)\, f(\varepsilon)\, g\,(\dot{\varepsilon}) \begin{bmatrix} \cos^2\theta & \cos\theta\sin\theta \\ \cos\theta\sin\theta & \sin^2\theta \end{bmatrix} \mathrm{d}\theta, \tag{19}$$

where ε is related to the Green–Lagrange strain tensor $\mathbf{E}$ by $\varepsilon = E_{11}\cos^2(\theta) + E_{22}\sin^2(\theta) + 2E_{12}\sin(\theta)\cos(\theta)$ and the quantity $\bar{T}$ denotes the typical magnitude of SF isometric contraction in fibroblasts. Note that the value of ϕ^{p} for different directions is determined from the knowledge of the structure's tensor $\mathbf{\Phi}^{\mathrm{p}}$ as described in [14].

A particularity of the preceding model of cell contraction is that it generates a positive feedback mechanism between fiber contraction and formation in the direction in which fiber shortening is mostly resisted. For instance, when cells adhere to a stiff substrate, their contraction only generates little deformation, which according to the tension–velocity curve enables SF to keep a level of isometric contraction. The presence of such a contraction consequently promotes more SF formation in this particular direction as described by the mechanosensitive formation model of (16). Inversely, a cell adhering to a soft substrate generates a significant amount of negative strains as a result of contraction. This results in switching the strain rate to the left of the tension–velocity curve in Figure 4 and thus decreasing the magnitude of SF contraction. Ultimately, this is translated into a drop in the rate of fiber formation and a loss of SF density.

3. GOVERNING EQUATIONS FOR THE CELL–SUBSTRATE INTERACTION PROBLEM

We now turn to the formulation of the interactions between cells and their mechanical environment. We particularly concentrate on the problem of cells lying on a two-dimensional elastic substrate, a situation that often arises both *in vivo* and in experiments.

3.1. Substrate elasticity

The mechanical behavior of the substrate is known to be an important factor driving cell morphology, contraction, and structure [27, 31, 39–41]. Although this behavior can be extremely complex, involving nonlinear elasticity, viscous effects, and inelasticity, the present work concentrates on the case of a simple linear isotropic elastic material with varying stiffness. Describing substrate deformation in terms of a displacement field $\mathbf{u}^{\mathrm{s}}$, one can introduce a rate of deformation and an objective rate for the substrate Cauchy stress $\mathbf{T}^{\mathrm{s}}$ in a similar form as that shown in (12). In other words, substrate elasticity is described in terms of two parameters (λ^{s}, μ^{s}) or equivalently by the set (E^{s}, ν^{s}) denoting Young's modulus and Poisson's ratio, respectively. It is finally straightforward to show that substrate equilibrium is written in terms of the divergence of the Cauchy stress as

$$\nabla \cdot \mathbf{T}^{\mathrm{s}} + \mathbf{b}^{\mathrm{s}} = \mathbf{0}, \tag{20}$$

where $\mathbf{b}^{\mathrm{s}}$ represents the body force vector in the substrate. In the following analysis, we assume that the substrate consists of a very thin layer that can be modeled in plane stress conditions. Although this situation may not accurately represent actual experimental conditions, the assumption is not expected to affect the main trends exhibited by cell in terms of different substrate elasticities.

3.2. Adhesion complexes

Cell–substrate adhesion is provided by the attachment between transmembrane molecules (known as integrins) and molecular complex (the ligands) lying on the surface of the substrate (Figure 5). Integrins easily diffuse through the cell membrane [42] to attach to free ligands on the substrate. It is thus realistic to assume that the magnitude of the adhesive force $\mathbf{t}_{\mathrm{a}}$ per unit area is directly related to the density η_{l} of ligands on the substrate by

$$\mathbf{t}_{\mathrm{a}} = \eta_{\mathrm{l}}\mathbf{f}_{\mathrm{a}}, \tag{21}$$

DOI: 10.1002/nme

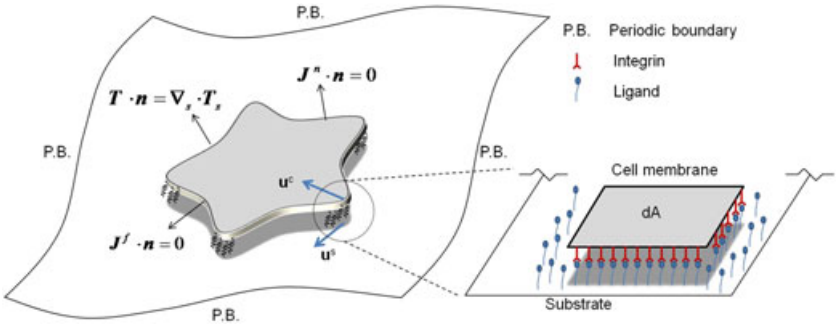

Figure 5. The general details of adhesion complexes between cell and substrate combined of integrins and ligands; together with the boundary conditions applied to cell and substrate.

where η_l denotes the number of ligands per unit substrate area and $\mathbf{f}_a$ is the force in a single ligand–integrin complex. Further assuming that the mechanical behavior of a ligand–integrin complex is represented by a linear force–separation relation with stiffness K_{li}, the continuum traction force (per unit area) is given by

$$\mathbf{t}_a = K_a \left(\mathbf{u}^c - \mathbf{u}^s\right), \quad \text{where} \quad K_a = \eta_l K_{li}, \tag{22}$$

where the term $\mathbf{u}^c - \mathbf{u}^s$ represents the separation between the cell membrane and the substrate surface. The preceding equation clearly states the stiffness of the adhesion stiffness increases linearly with ligand density. It also shows that if no ligands are present $\eta_l = 0$, no cell–substrate adhesion is possible ($\mathbf{t}_a = 0$).

3.3. Summary of the governing equations under plane stress conditions: strong form

Considering that the cell and the substrate lie in the x–y plane of the (x, y, z)-coordinate system, plane stress conditions imply that stress components associated with the z-direction vanish. In addition, adhesion forces $\mathbf{t}_a$ acting on the bottom cell surface and the top substrate surface are represented by vectors in the x–y plane and are equivalent to 'body forces' acting in the cell and the substrate with equal magnitude but in opposite directions. In other words, the body forces $\mathbf{b}$ and $\mathbf{b}^s$ appearing in (8) and (20) are replaced by adhesive forces such that the mechanical equilibrium for cell and substrate is written as follows:

$$\nabla \cdot \mathbf{T}^s + \mathbf{t}_a = 0 \ \text{ in } \ \Omega^s \qquad \mathbf{u}^s = \mathbf{u}^* \ \text{ on } \ \Gamma^s, \tag{23}$$

$$\nabla \cdot \mathbf{T} - \mathbf{t}_a = 0 \ \text{ in } \ \Omega^c \qquad \mathbf{T} \cdot \mathbf{n} = \nabla_\sigma \cdot \mathbf{T}_\sigma \ \text{ on } \ \Gamma^c. \tag{24}$$

Note that the elastic constitutive relations are affected by the plane stress conditions. For clarity, a detailed description of these equations is left in Appendix A. In addition, one can show that mass conservation equations ((2) and (3)) in the cell domain Ω^c under plane stress conditions take the form

$$\alpha \, \nabla \cdot \mathbf{v} + \beta \, \dot{p} + \nabla \cdot \mathbf{J}^f + \nabla \cdot \mathbf{J}^m = 0 \ \text{ in } \Omega^c \qquad \mathbf{J}^m \cdot \mathbf{n} = 0 \ \text{ on } \ \Gamma^c, \tag{25}$$

$$\frac{D\phi^f}{Dt} + \alpha \phi^f \, \nabla \cdot \mathbf{v} + \beta \phi^f \dot{p} + \nabla \cdot \mathbf{J}^f = 0 \ \text{ in } \Omega^c \qquad \mathbf{J}^f \cdot \mathbf{n} = 0 \ \text{ on } \ \Gamma^c, \tag{26}$$

where coefficients α and β depend on Poisson's ratio ν and Young's modulus E of the cell's cytoskeleton as follows (Appendix A):

$$\alpha = \frac{1 - 2\nu}{1 - \nu} \quad \text{and} \quad \beta = \frac{(1 + \nu)(1 - 2\nu)}{E(1 - \nu)}.$$

Similarly, the SF evolution equation (5) becomes

$$\frac{D\boldsymbol{\Phi}^p}{Dt} + \boldsymbol{\Phi}^p \, \alpha \, \nabla \cdot \mathbf{v} + \boldsymbol{\Phi}^p \, \beta \, \dot{p} = \boldsymbol{\Pi}^p \ \text{ in } \ \Omega^c. \tag{27}$$

DOI: 10.1002/nme

In the end, the five equations ((23), (24), (25), (26), and (27)) subjected to the given boundary conditions can be solved to determine five unknowns that consist of the following: (1) the displacement field $\mathbf{u}^{\mathrm{s}}(\mathbf{X},t)$ in the substrate domain Ω^{s}; (2) the displacement field $\mathbf{u}(\mathbf{X},t)$ in the cell domain Ω^{c}; (3) the cytosol volume fraction $\phi^{\mathrm{f}}(\mathbf{X},t)$ in Ω^{c}; (4) the monomer volume fraction $\phi^{\mathrm{m}}(\mathbf{X},t)$ in Ω^{c}; and finally, (5) the structure tensor $\mathbf{\Phi}^{\mathrm{p}}(\mathbf{X},t)$ describing the SF distribution in Ω^{c}.

3.4. Summary of the governing equations: weak form

The earlier coupled differential equations constitute a highly nonlinear system whose solution lies in the three-dimensional space (x,y,t). A numerical strategy based on the FEM is therefore necessary to obtain a solution in the most general case. Such a formulation requires that governing equations are rewritten in an integral form (or weak form) as described in this section. For this, we introduce arbitrary admissible weighting functions denoted by scalars functions θ and λ, vector functions $\boldsymbol{\omega}$ and $\boldsymbol{\omega}^{\mathrm{s}}$, and a second-order tensor function $\mathbf{\Lambda}$. Multiplying each governing equation ((23), (24), (25), (26), and (27)) with a corresponding weight function and integrating over their associated domain, we obtain five scalar equations as follows:

$$\int_{\Omega^{\mathrm{s}}} \boldsymbol{\omega}^{\mathrm{s}} \cdot (\nabla \cdot \mathbf{T}^{\mathrm{s}} + \mathbf{t}_{\mathrm{a}})\ \mathrm{d}\Omega^{\mathrm{s}} = 0, \tag{28}$$

$$\int_{\Omega^{\mathrm{c}}} \boldsymbol{\omega} \cdot [\nabla \cdot (\mathbf{T}^{\mathrm{c}} + \mathbf{T}^{\mathrm{p}} - p\mathbf{I}) - \mathbf{t}_{\mathrm{a}}]\ \mathrm{d}\Omega^{\mathrm{c}} = 0, \tag{29}$$

$$\int_{\Omega^{\mathrm{c}}} \theta \left[\alpha\ \nabla \cdot \mathbf{v} + \ \beta\ \dot{p} + \nabla \cdot \mathbf{J}^{\mathrm{f}} + \nabla \cdot \mathbf{J}^{\mathrm{m}} \right] \mathrm{d}\Omega^{\mathrm{c}} = 0, \tag{30}$$

$$\int_{\Omega^{\mathrm{c}}} \lambda \left[\frac{D\phi^{\mathrm{f}}}{Dt} + \phi^{\mathrm{f}}\ \alpha\ \nabla \cdot \mathbf{v} + \phi^{\mathrm{f}}\ \beta\ \dot{p} + \nabla \cdot \mathbf{J}^{\mathrm{f}} \right] \mathrm{d}\Omega^{\mathrm{c}} = 0, \tag{31}$$

$$\int_{\Omega^{\mathrm{c}}} \mathbf{\Lambda} : \left[\frac{D\mathbf{\Phi}^{\mathrm{p}}}{Dt} + \mathbf{\Phi}^{\mathrm{p}}\ \alpha\ \nabla \cdot \mathbf{v} + \mathbf{\Phi}^{\mathrm{p}}\ \beta\ \dot{p} - \mathbf{\Pi}^{\mathrm{p}} \right] \mathrm{d}\Omega^{\mathrm{c}} = 0. \tag{32}$$

Integrating by part and applying the divergence theorem, we may rewrite the weak form in the following more convenient form:

$$\int_{\Omega^{\mathrm{s}}} \nabla \boldsymbol{\omega}^{\mathrm{s}} : \mathbf{T}^{\mathrm{s}}\ \mathrm{d}\Omega^{\mathrm{s}} - \int_{\Omega^{\mathrm{c}}} \boldsymbol{\omega}^{\mathrm{s}} \cdot \mathbf{t}_{\mathrm{a}}\ \mathrm{d}\Omega^{\mathrm{c}} = 0, \tag{33}$$

$$\int_{\Omega^{\mathrm{c}}} \nabla \boldsymbol{\omega} : (\mathbf{T}^{\mathrm{c}} + \mathbf{T}^{\mathrm{p}} - p\mathbf{I})\ \mathrm{d}\Omega^{\mathrm{c}} + \int_{\Omega^{\mathrm{c}}} \boldsymbol{\omega} \cdot \mathbf{t}_{\mathrm{a}}\ \mathrm{d}\Omega^{c} + \int_{\Gamma^{\mathrm{c}}} (\mathbf{P} \cdot \nabla \boldsymbol{\omega} \cdot \mathbf{P}) : \mathbf{T}_{\sigma}\ \mathrm{d}\Gamma^{\mathrm{c}} = 0, \tag{34}$$

$$\int_{\Omega^{\mathrm{c}}} \theta\ (\alpha\ \nabla \cdot \mathbf{v} + \ \beta\ \dot{p})\ \mathrm{d}\Omega^{\mathrm{c}} + \int_{\Omega^{\mathrm{c}}} \nabla\theta \cdot \frac{\kappa}{\mu} \nabla p\ \mathrm{d}\Omega^{\mathrm{c}} + \int_{\Omega^{\mathrm{c}}} \nabla\theta \cdot \left(\frac{\phi^{\mathrm{m}}}{\phi^{\mathrm{f}}} \frac{\kappa}{\mu} \nabla p + D\ \nabla\phi^{\mathrm{m}} - \frac{\phi^{\mathrm{m}}}{\phi^{\mathrm{f}}} D\ \nabla\phi^{\mathrm{f}} \right) \mathrm{d}\Omega^{\mathrm{c}} = 0, \tag{35}$$

$$\int_{\Omega^{\mathrm{c}}} \lambda \dot{\phi}^{\mathrm{f}}\ \mathrm{d}\Omega^{\mathrm{c}} + \int_{\Omega^{\mathrm{c}}} \lambda\phi^{\mathrm{f}}\ (\alpha\ \nabla \cdot \mathbf{v} + \ \beta\ \dot{p})\ \mathrm{d}\Omega^{\mathrm{c}} + \int_{\Omega^{\mathrm{c}}} \nabla\lambda \cdot \frac{\kappa}{\mu} \nabla p\ \mathrm{d}\Omega^{\mathrm{c}} = 0, \tag{36}$$

$$\int_{\Omega^{\mathrm{c}}} \mathbf{\Lambda} : \dot{\mathbf{\Phi}}^{\mathrm{p}}\ \mathrm{d}\Omega^{\mathrm{c}} + \int_{\Omega^{\mathrm{c}}} \mathbf{\Lambda} : \mathbf{\Phi}^{\mathrm{p}}\ (\alpha\ \nabla \cdot \mathbf{v} + \ \beta\ \dot{p})\ \mathrm{d}\Omega^{\mathrm{c}} - \int_{\Omega^{\mathrm{c}}} \mathbf{\Lambda} : \left[\frac{M^{\mathrm{p}}}{M^{\mathrm{m}}} \left(\frac{1}{2} k_0^{\mathrm{f}} \mathbf{I} + k_1^{\mathrm{f}} \mathbf{T}^{\mathrm{p}} \right) \frac{\phi^{\mathrm{m}}}{\phi^{\mathrm{f}}} - k_0^{\mathrm{d}} \mathbf{\Phi}^{\mathrm{p}} \right] \mathrm{d}\Omega^{\mathrm{c}} = 0. \tag{37}$$

The preceding system of equation is then linearized to obtain a numerical solution using the modified Newton–Raphson iterative method. In a nutshell, a function f is linearized about its current value according to $f = \tilde{f} + \delta f$, where $\tilde{f}$ is the value of f obtained in the last increment and δf defines the partial change in f during the current time increment. The solution may then be obtained with an incremental method whose details are given in Appendix B.

DOI: 10.1002/nme

4. LEVEL SET–EXTENDED FEM FORMULATION

4.1. Numerical strategy for cell–substrate interactions

From a numerical viewpoint, the cell–substrate interaction under plane stress assumptions involves two superposed domains Ω^s and Ω^c, of arbitrary shapes, on which different, but interacting, fields must be computed (Figure 1). To solve such a problem, two strategies may be adopted. The first would consist in introducing different discretizations for each domain, on which solutions would be computed separately but can interact through a numerical treatment of the interactions at cell–substrate adhesions. The second, introduced in this paper, only requires a single discretization, used for both cell and substrate. In this approach, whereas the substrate domain Ω^s is entirely contained in the computational domain, the cell domain Ω^c is defined in terms of a level set function that defines the arbitrary contour of the cell.

Referring to Figure 6a, the level set function $\phi(\mathbf{X})$ is a function of space (in the undeformed configuration) that is represented by a two-dimensional surface in a three-dimensional space. The two-dimensional morphology of the cell is then defined as the intersection of this surface with the x–y plane of the cell (Figure 6a). The function ϕ is chosen such that its sign is opposite in two sides of the cell boundary, which enables a clear definition concerning the location of material point P located at $\mathbf{X}$ with respect to the cell domain:

$$\text{if } \phi(\mathbf{X}) > 0, \quad P \in \Omega^c, \tag{38}$$

$$\text{if } \phi(\mathbf{X}) = 0, \quad P \in \Gamma^c, \tag{39}$$

$$\text{if } \phi(\mathbf{X}) < 0, \quad P \notin \Omega^c. \tag{40}$$

In addition, the level set function enables the definition of the unit vector $\mathbf{n}_0$ that is normal to the cell boundary Γ^c in its original configuration,

$$\mathbf{n}_0(\mathbf{X}) = \frac{\nabla_{\mathbf{X}}\phi(\mathbf{X})}{||\nabla_{\mathbf{X}}\phi(\mathbf{X})||}, \tag{41}$$

where $\nabla_{\mathbf{X}}$ denotes the gradient with respect to the initial coordinate $\mathbf{X}$ and $||\cdot||$ denotes the L_2 norm. This strategy enables us to define arbitrary cell morphologies independently from finite element discretization. Furthermore, nodes located outside of the cell domain are only associated with substrate displacement $\mathbf{u}^s$ whereas nodes that are located in Ω^c are associated with degrees of freedom related to both substrate ($\mathbf{u}^s$) and cell ($\mathbf{u}$, p, ϕ^m, $\boldsymbol{\Phi}^p$). This approach, when combined with the XFEM, has several advantages:

- Complex cell geometries may naturally be handled independently of finite element discretization. When interacting with their mechanical environment, cells can take very complex

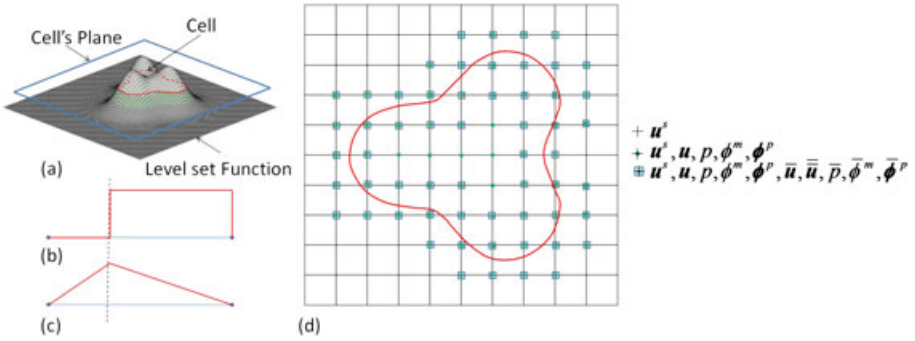

Figure 6. (a) Example of a level set function used to describe cell geometry and (b) heavy side and (c) ridge functions used to enrich the finite element interpolation. (d) Degrees of freedom associated with nodes inside and outside the cell. The enriched nodes are shown with blue squares.

DOI: 10.1002/nme

morphologies. In numerical simulations, this leads to significant issues with meshing, especially when three-dimensional shapes are considered. The presented method circumvents this issue by defining a shape geometry using a mesh-independent level set function. We note that this approach is also in line with recent experimental techniques that evaluate the evolution of cell morphology in tissue with level set functions [23]. A combination of the presented numerical method with such techniques will eventually lead to a fully integrated experimental modeling approach to improve our understanding of cells and tissues.

- The XFEM enrichment functions enable the incorporation of the stiffness of the cortical membrane surrounding the cell; this feature is known to be critical to realistically capturing cell morphology. The XFEM contributes a very natural framework to integrate the equations of membrane elasticity on an interface defined by a level set function. We have previously shown in [15] that such a formulation was accurate in capturing the effect of cells' cortical membrane on their overall deformation.
- Because cell and substrate domains are discretized with the same mesh, the numerical treatment of cell–substrate cohesion is accurate and simple. This approach circumvents many difficulties associated with implementing cohesive models between two domains with different discretization [16–19].
- The problem of cell evolution and growth can naturally be incorporated in the formulation by using level set evolution equations . This method has been previously used to capture the changes in evolving interfaces between two incompressible constituents of a two-phase flow [43–45] and the growth of biofilms [24]. The coupling between these methods and the proposed approach is likely to yield a powerful numerical tool to describe important cellular phenomena such as cell spreading, growth, and migration.

4.2. Multifield extended finite element formulation

The main issue with the aforementioned method is that continuum fields associated with the cell domain are typically discontinuous across the cell boundary Γ^{c}. For instance, a continuum field $\mathbf{f}$ associated with the cell domain (this can be $\mathbf{u}$, p, ϕ^{m}, or $\mathbf{\Phi}^{\mathrm{p}}$) is typically nonzero in Ω^{c} but vanishes outside Ω^{c}, therefore creating a jump in $\mathbf{f}$ across Γ^{c}. This generally poses a problem with the standard finite element method as shape functions are continuous within an element, and yet, Γ^{c} exists within element domains (Figure 6d). To circumvent this obstacle, the proposed approach uses the XFEM methodology [20, 46] for its strength in describing various types of discontinuities within element domains [21, 22, 47–49]. In this context (Figure 6d), the elements cut by the level set and their nodes are considered as enriched elements/nodes. To introduce discontinuities in a continuum field $\mathbf{f}$ (denoted as strong discontinuity) and its gradient (denoted as weak discontinuity) across the cell boundary, fictitious degrees of freedom $\bar{\mathbf{f}}$ and $\bar{\bar{\mathbf{f}}}$ are added to the enriched nodes such that a numerical approximation $\tilde{\mathbf{f}}$ of the function $\mathbf{f}$ can be introduced using conventional finite element shape functions,

$$\tilde{\mathbf{f}}(\mathbf{x}) = \sum_{I=1}^{n} \mathbf{N}_I(\mathbf{x})\mathbf{f}_I + \sum_{J=1}^{m} \mathbf{N}_J(\mathbf{x})(H(\mathbf{x}) - H(\mathbf{x}_J))\bar{\mathbf{f}}_J + \sum_{J=1}^{m} \mathbf{N}_J(\mathbf{x})\,(\chi(\mathbf{x}) - \chi(\mathbf{x}_J))\,\bar{\bar{\mathbf{f}}}_J, \tag{42}$$

where $\mathbf{N}_I(\mathbf{x})$ are shape functions associated with node I. The matrix $\mathbf{N}_I$ has the following form:

$$\mathbf{N}_I(\mathbf{x}) = \begin{bmatrix} N_I(\mathbf{x}) & 0 \\ 0 & N_I(\mathbf{x}) \end{bmatrix}. \tag{43}$$

In (42), $\mathbf{N}_J(\mathbf{x})$ are ordinary shape functions of the enriched nodes, that is, the nodes of the elements cut by level set function, whereas n and m give the total number of nodes and the number of enriched nodes per element, respectively. In addition, the Heaviside and ridge functions, denoted as $H(\mathbf{x})$ and $\chi(\mathbf{x})$, take the following form:

$$H(\mathbf{X}) = \begin{cases} 1 & \phi(\mathbf{X}) > 0 \\ 0 & \phi(\mathbf{X}) < 0 \end{cases} \quad \text{and} \quad \chi(\mathbf{X}) = |\phi(\mathbf{X})|. \tag{44}$$

DOI: 10.1002/nme

The function $H(\mathbf{x})$ is used to introduce a jump in the fields $\dot{\mathbf{u}}^{\mathrm{c}}$, $\dot{p}, \dot{\phi}^{\mathrm{m}}$, and $\dot{\mathbf{\Phi}}^{\mathrm{p}}$ across the cell's membrane, whereas the ridge function is used to define discontinuities in their spatial derivative [21, 50]. A one-dimensional representation of the Heaviside and ridge functions is provided in Figure 6b and c

4.3. Discretization and time integration

The linearized finite element equation is obtained by substituting the XFEM approximation (42) corresponding to each continuum field $\mathbf{u}^{\mathrm{s}}, \mathbf{u}, p, \phi^{\mathrm{m}}$, and $\mathbf{\Phi}^{\mathrm{p}}$ into the linearized weak-form equations ((33)–(37)). Note that the enrichment functions are only used for elements that are cut by the cell's interface Γ^{c}. In these elements, whereas all fields are enriched with a strong discontinuity, only the cell's displacement field $\mathbf{u}$ is enriched with the Ridge function (weak discontinuity). Indeed, the weakly discontinuous displacement field is only important to capturing the jump in strain between the cell and its surrounding due to surface tension [15]. Furthermore, a mixed-element formulation is adopted from quadratic, bilinear, four-point Lagrange interpolation functions to approximate cytosol pressure p, G-actin monomer volume fraction ϕ^{m}, and F-actin SF volume fraction $\mathbf{\Phi}^{\mathrm{p}}$ and from nine-point Lagrange interpolation functions to approximate the displacement field $\mathbf{u}$. The nodal values of the continuum fields in element e are then given by a vector $\mathbf{U}^e$,

$$\mathbf{U}_I^e = \left[\begin{array}{cccc} \mathbf{u}_I^{\mathrm{s},e} & \mathbf{u}_I^e & \mathbf{p}_I^e & \boldsymbol{\phi}_I^{\mathrm{m},e} \quad \mathbf{\Phi}_I^{\mathrm{p},e} \end{array} \right]^{\mathrm{T}}, \tag{45}$$

where I denotes the node number in the local element numbering scheme. In other words, $I = 1, \ldots, 4$ for four-node elements and $I = 1, \ldots, 9$ for nine-node elements. Finite element approximation in an element is then expressed in terms of these nodal values by (42). After substitution of the aforementioned approximation into the weak-form equations, integration is performed numerically by using a nine-point quadrature rule for conventional elements while considering the following treatment for enriched elements. Because enriched elements are cut into two domains by interface Γ^{c}, a number of sub-triangles can be constructed on each side of the interface. Element integration is thus decomposed into integration on each of these sub-triangles by using a 13-point Gauss rule for maximum accuracy. In addition, numerical integration along the cell's surface Γ^{c} is carried out using a one-dimensional three-point Gauss rule. For more details of using sub-triangles and integration on surface, the reader is referred to [49, 51]. After a long but straightforward calculation for which the details are given in Appendix C, we find that the final XFEM equation takes the form

$$\mathbf{C} \cdot \dot{\mathbf{U}} + \mathbf{K} \cdot \delta\mathbf{U} + \mathbf{F} = \mathbf{0}, \tag{46}$$

where $\mathbf{U}$ denotes the global displacement vector. Indeed, the global force vector, as well as the tangent and damping matrices, is assembled from their element counterparts as follows:

$$\mathbf{F} = \mathop{\mathscr{A}}_{e=1}^{nel} \mathbf{F}^e \qquad \mathbf{K} = \mathop{\mathscr{A}}_{e=1}^{nel} \mathbf{K}^e \quad \text{and} \quad \mathbf{C} = \mathop{\mathscr{A}}_{e=1}^{nel} \mathbf{C}^e. \tag{47}$$

Here, $\mathscr{A}$, e and nel denote the assembly operation, element number, and the number of elements, whereas the element force vector, the damping matrix, and the stiffness matrix are given by the following:

$$\mathbf{F} = \begin{bmatrix} \mathbf{F}^{u^{\mathrm{s}}} \\ \mathbf{F}^{u} \\ \mathbf{F}^{\mathrm{f}} \\ \mathbf{F}^{\mathrm{m}} \\ \mathbf{F}^{\mathrm{p}} \end{bmatrix}; \mathbf{C} = \begin{bmatrix} 0 & 0 & 0 & 0 & 0 \\ 0 & \mathbf{C}^{uu} & 0 & 0 & 0 \\ 0 & \mathbf{C}^{\mathrm{f}u} & \mathbf{C}^{\mathrm{ff}} & 0 & 0 \\ 0 & \mathbf{C}^{\mathrm{m}u} & \mathbf{C}^{\mathrm{mf}} & \mathbf{C}^{\mathrm{mm}} & \mathbf{C}^{\mathrm{mp}} \\ 0 & \mathbf{C}^{\mathrm{p}u} & \mathbf{C}^{\mathrm{pf}} & 0 & \mathbf{C}^{\mathrm{pp}} \end{bmatrix}; \mathbf{K} = \begin{bmatrix} \mathbf{K}^{\mathrm{ss}} & \mathbf{K}^{\mathrm{s}u} & 0 & 0 & 0 \\ \mathbf{K}^{u\mathrm{s}} & \mathbf{K}^{uu} & \mathbf{K}^{u\mathrm{f}} & 0 & \mathbf{K}^{u\mathrm{p}} \\ 0 & \mathbf{K}^{\mathrm{f}u} & \mathbf{K}^{\mathrm{ff}} & \mathbf{K}^{\mathrm{fm}} & \mathbf{K}^{\mathrm{fp}} \\ 0 & 0 & \mathbf{K}^{\mathrm{mf}} & 0 & 0 \\ 0 & \mathbf{K}^{\mathrm{p}u} & \mathbf{K}^{\mathrm{pf}} & \mathbf{K}^{\mathrm{pm}} & \mathbf{K}^{\mathrm{pp}} \end{bmatrix}. \tag{48}$$

A precise form of the components appearing in the preceding equations are given in Appendix D. Equation (46) is solved using a nonlinear updated Lagrangian formulation [52] following the algorithm presented in Figure 7. Furthermore, time integration is performed using a backwards Euler

DOI: 10.1002/nme

- Define the total time t_{tot} and the time step Δt.
- Initialize the unknowns
- Start time steps (t)
  - Start nonlinear iterative loop (i)
    - ◇ Start loop on gauss points for each element (e)
      - ▷ Update gauss point values such as stress and strain
      - ▷ Calculate $\mathbf{K}_{t+\Delta t}^{i-1,e}$, $\mathbf{C}_{t+\Delta t}^{i-1,e}$, *and* $\mathbf{F}_{t+\Delta t}^{i-1,e}$ for each element
    - ◇ End gauss point and element loop
    - ◇ Assembly of $\mathbf{K}_{t+\Delta t}^{i-1,e}$, $\mathbf{C}_{t+\Delta t}^{i-1,e}$, *and* $\mathbf{F}_{t+\Delta t}^{i-1,e}$
    - ◇ Apply boundary conditions
    - ◇ Solve for $\delta\dot{\mathbf{U}}$: $\left(\mathbf{C}_{t+\Delta t}^{i-1} + \Delta t.\mathbf{K}_{t+\Delta t}^{i-1}\right).\delta\dot{\mathbf{U}}^i = -\left(\mathbf{F}_{t+\Delta t}^{i-1} + \mathbf{C}_{t+\Delta t}^{i-1} \cdot \dot{\mathbf{U}}_{t+\Delta t}^{i-1}\right)$
    - ◇ Update the unknowns: $\dot{\mathbf{U}}_{t+\Delta t}^{i} = \dot{\mathbf{U}}_{t+\Delta t}^{i-1} + \delta\dot{\mathbf{U}}^i$ and $\mathbf{U}_{t+\Delta t}^{i} = \mathbf{U}_{t}^{i} + \Delta t \cdot \dot{\mathbf{U}}_{t+\Delta t}^{i}$
  - End nonlinear iterative loop if norm$\left(\delta\dot{\mathbf{U}}^i\right) <$ tol
  - Update nodal coordinates of mesh
  - Update the cell's surface shape
- End time steps

Figure 7. The nonlinear updated Lagrangian algorithm used to solve Equation (51).

integration scheme that approximates a field at a given time step from the approximate derivative at the next time step. This is written as

$$\delta\mathbf{U} = \delta\dot{\mathbf{U}} \cdot \Delta t, \tag{49}$$

where Δt denotes the time increment. Because of the inherent nonlinearity of the contraction problem, the solution for $\dot{\mathbf{U}}(t + \Delta t)$ is solved for iteratively at time increment $t + \Delta t$. The value $\dot{\mathbf{U}}^i(t + \Delta t)$ at the ith iteration is calculated by

$$\dot{\mathbf{U}}^i(t + \Delta t) = \dot{\mathbf{U}}^{i-1}(t + \Delta t) + \delta\dot{\mathbf{U}}^i, \tag{50}$$

substituting Equations (49) and (50) into Equation (46); the iterative rate vector $\delta\dot{\mathbf{U}}^i$ is computed as

$$\left(\mathbf{C}_{t+\Delta t}^{i-1} + \Delta t.\mathbf{K}_{t+\Delta t}^{i-1}\right).\delta\dot{\mathbf{U}}^i = -\left(\mathbf{F}_{t+\Delta t}^{i-1} + \mathbf{C}_{t+\Delta t}^{i-1} \cdot \dot{\mathbf{U}}_{t+\Delta t}^{i-1}\right) \equiv \mathbf{H}_{t+\Delta t}^{i-1} \tag{51}$$

where the notation $\mathbf{H}$ is used for residual vector. Iterations are then repeated until the norm of the partial rate vector $|\delta\mathbf{U}^i| < tol$ where tol is a small tolerance.

5. NUMERICAL INVESTIGATION OF CELL CONTRACTION ON ELASTIC SUBSTRATES

The proposed numerical approach is now assessed in several ways. First, we consider the case of an originally square-shaped cell, attached to its underlying substrate through focal adhesion at its corners. The numerical behavior of the system, as well as convergence studies are presented. We then build upon this analysis to investigate the contractile behavior and structural evolution of cells sitting on substrate with varying elasticity and compare our predictions with experimental observations. Furthermore, taking advantage of the level set formulation, we investigate the effect of cell morphology on its structural organization as well as on the deformation of the substrate. Finally, we assess the role of the cortical membrane stiffness on SF formation and substrate stresses. The presented simulations are obtained by using a set of physiologically relevant parameters that are characteristic of fibroblasts (Table I).

5.1. Convergence analysis

In this section, we propose to assess the convergence of the solution method by considering the particular problem of the evolution of a square cell interacting with an elastic substrate through adhesion regions located near its four corners (Figure 10a). For all analyses, Young's modulus of

DOI: 10.1002/nme

Table I. Parameters used in the simulations.

Definition	Symbol	Value	Unit	Reference
Cytosol volume fraction	ϕ^{c}	70	%	[53]
Cytoskeleton volume fraction	ϕ^{s}	25	%	n/a
F + G actin volume fraction	$\phi^{\mathrm{m}} + \phi^{\mathrm{p}}$	5	%	n/a
Rate of SF formation	k_0^{f}	0.0001	s^{-1}	[54]
Mechanosensitive rate of SF formation	k_1^{f}	0.05	s^{-1}	[54]
Rate of SF dissociation	k_0^{d}	0.1	s^{-1}	[54]
Cytoskeleton permeability	κ/μ	$1 \cdot 10^{-15}$	$\mathrm{m}^4/\mathrm{N} \cdot \mathrm{s}$	[55]
G-actin diffusion constant	D	$1 \cdot 10^{-5}$	m^2/s	[54]
Young's modulus	E	70	Pa	[12]
Poisson's ratio	ν	0.3		[12]
Fiber maximum tensile stress	$\bar{T}$	20,000	Pa	[33, 56, 57]
Reference strain rate (Equation (17))	$\dot{\varepsilon}_0$	0.01	s^{-1}	[12]
Reference active strain (Equation (18))	ε_0	0.1		[37]
Reference passive strain (Equation (18))	ε_1	0.15		[37]
F/G molar mass ratio	$M^{\mathrm{p}}/M^{\mathrm{m}}$	100		n/a
F/G true density ratio	$\rho_R^{\mathrm{p}}/\rho_R^{\mathrm{m}}$	1		n/a
Integrin density	η_{l}	1000	m^{-2}	n/a
Single adhesion complex stiffness	K_{li}	10^7	N/m	n/a

SF, stress fiber.

the substrate is chosen to be $E^{\mathrm{s}} = 100$ Pa, and initial conditions are such that no SFs are present in the cell at time $t = 0$ (i.e., actin is present in its monomer form only). Convergence is then evaluated at steady state (when both chemical and mechanical equilibrium are reached) with respect to mesh size and Newton iteration number at fixed time steps. In all cases, the results are compared with ordinary FEM based on the discretization depicted in Figure 10. The figure particularly shows the different meshes used to describe substrate and cell domains, as well as the location of the adhesion complexes connecting them.

Convergence with respect to mesh size is first evaluated by studying the change in the magnitude of a relevant global quantity G with increasing element number. Here, we choose G as the average SF volume fraction at steady state,

$$G = \frac{1}{A_0^{\mathrm{c}}} \int_{\Omega^{\mathrm{c}}} \mathrm{trace}\left(\mathbf{\Phi}^{\mathrm{p}}\left(\mathbf{X}, t^{\mathrm{f}}\right)\right) \mathrm{d}\Omega^{\mathrm{c}}, \tag{52}$$

where A_0^{c} and t^{f} are the initial cell's area and the time at which the system has reached its steady-state solution, respectively. Furthermore, we introduce G_k as the value of G numerically obtained $k \times k$ square finite elements. As expected, the quantity G_k converges to a fixed point $G = 0.415\%$ and 0.410% for the XFEM and FEM simulations, respectively, as k increases (Figure 8a). This figure shows that for the particular problem of an initially square cell, FEM results generally display a slightly smaller numerical error than XFEM results. This error is attributed to the existence of sharp corners, which leads to small inaccuracies in the computation of the solution with the XFEM. Note that this issue may be resolved in the future by considering the effect of sharp angles within the XFEM enrichment functions. The rate of convergence of both the XFEM and the FEM was assessed with the formula

$$|G_k - G| \leqslant C \left(\frac{1}{k}\right)^q, \tag{53}$$

DOI: 10.1002/nme

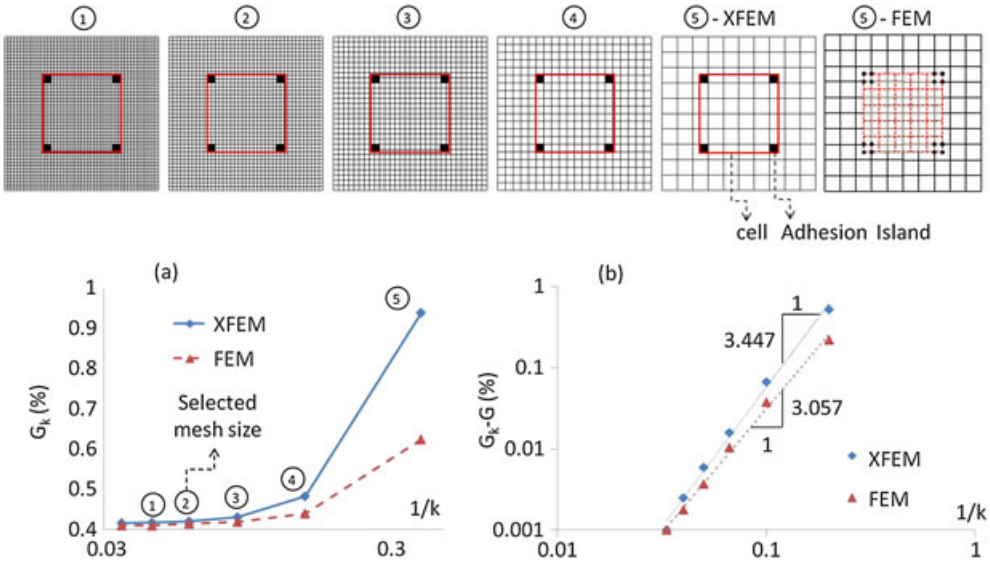

Figure 8. (a) Discretization convergence of the numerical extended FEM (XFEM) solution to estimate average SF volume fraction in cell by changing mesh size and comparison with ordinary FEM. (b) Proof of quadratic convergence of the discretization according to Equation (53) and comparison between the XFEM and the FEM.

where C is a chosen constant value and q is a positive integer that gives the rate of convergence with respect to spatial discretization. Figure 8b shows that in a log–log scale, the numerical error $E = |G_k - G|$ changes linearly as a function of $1/k$ such that the slope of the line exhibits the rate of convergence ($q = 3.447$ and 3.057 for the FEM and XFEM simulations, respectively). It is particularly interesting to see that the XFEM displays a slightly better rate of convergence than the FEM. In view of this result, the simulations presented in the remainder of the paper are based on a mesh of 20×20 elements (in the cell domain); this choice gave us an optimal combination of accuracy and numerical efficiency.

We also investigated the convergence of the presented numerical scheme in terms of iteration number by plotting the norm of the vector $\delta\mathbf{U}^i = |\mathbf{U}^i - \mathbf{U}|$ (defined in Equation (49)) in terms of the iteration number i for a fixed-term increment, where $\mathbf{U}^i$ and $\mathbf{U}$ denote the value of unknown vector at iteration i and its converged value for the same time step, respectively. As depicted in Figure 9, we observed a linear convergence rate, that is,

$$\lim_{i\to\infty} \frac{|\mathbf{U}^i - \mathbf{U}|}{|\mathbf{U}^{i-1} - \mathbf{U}|^q} = \mu, \tag{54}$$

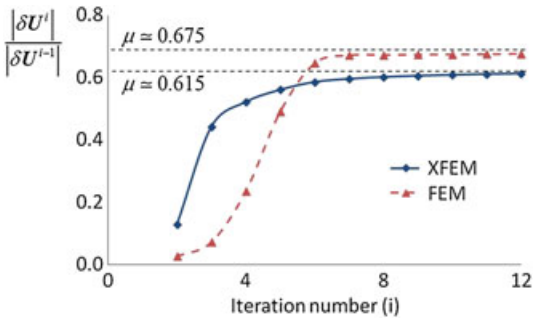

Figure 9. Linear convergence of the nonlinear solution method for the extended FEM (XFEM) and the ordinary FEM.

DOI: 10.1002/nme

where the parameters $\mu = 0.615$ and $\mu = 0.675$ were obtained for the XFEM and the FEM, respectively, for $q = 1$ [58]. Note that the values of the parameter μ for the FEM and the XFEM are calculated for the same time step, and the lower value of μ for the XFEM indicates a better rate of convergence in comparison with FEM.

5.2. *Effect of cell morphology on stress fiber development*

As noted in the previous section, one main advantage of using the XFEM–level set approach relies in that cell geometry can be defined independently from discretization. In this example, we take advantage of this capability to investigate the SF evolution in three cells, characterized by different geometries (square, rectangle, and triangle) and substrate adhesion (Figure 10a–c) on an elastic substrate whose elastic modulus is 100 Pa. Because of their simple geometries, square and rectangular cells can easily be handled with the ordinary FEM; for validation purposes, we therefore compute solutions using both the XFEM and the FEM, when subjected to the same element size. In addition, although initial conditions are the same as in the previous section, we applied periodic boundary conditions on the substrate domain to simulate an infinitely large domain with a periodic cell's structure. More details on this approach are given in [59].

Figure 10d–f shows the first stress invariant in the substrates due to cell contraction at steady state. These results clearly show that compressive state of stress beneath the cell and the tensile stress between cells (neighboring cells are represented by periodic boundary conditions). The importance of this formulation is clear as it is able to represent the interactions between cells of arbitrary shapes (information that can be obtained from imaging) and elastic substrates. Furthermore, SF distribution at steady state was obtained for each cell morphology (Figure 10g–i) and compared

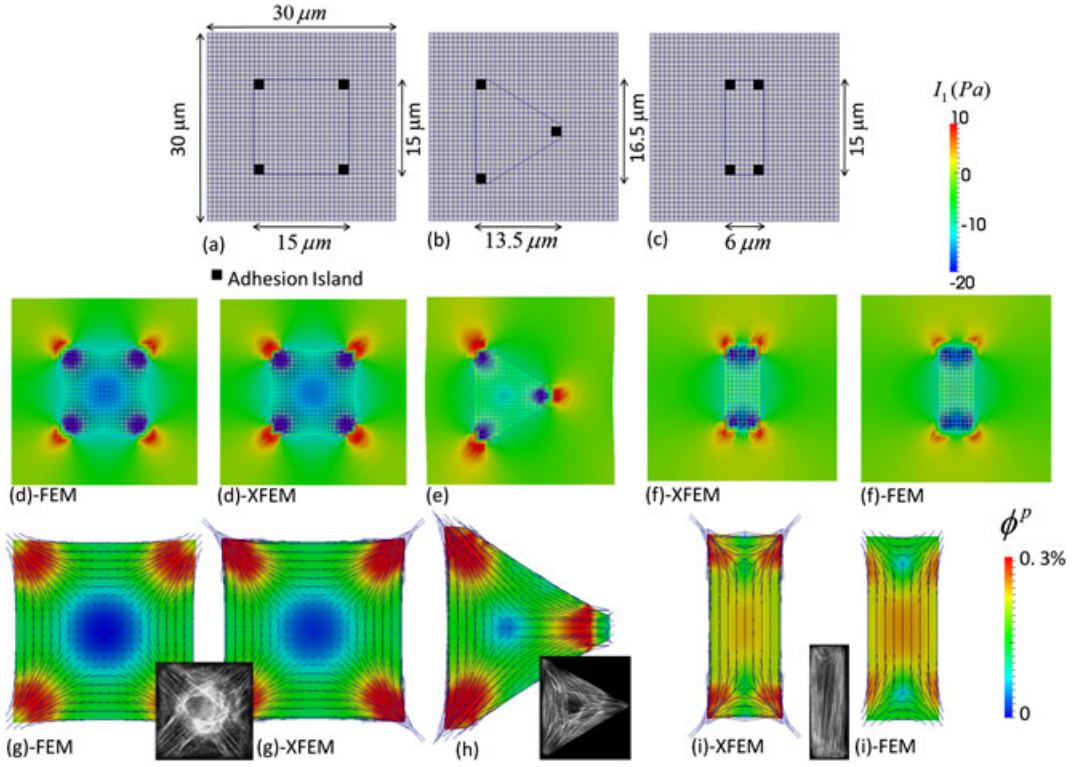

Figure 10. (a–c) Initial configurations of cells with different shapes on substrate. The dimensions of the adhesion island are 1.5 μm × 1.5 μm for all cases. In the ordinary FEM simulations, cell corner elements are attached to the substrate at nodal locations. (d–f) Deformed configuration of the cells together with the first invariant of the stress in the substrate for the extended FEM (XFEM) and the FEM. (g–i) Deformed configuration of cells with different shapes together with their stress fiber orientation in steady state to be compared with ordinary FEM and the experimental results of SF formation in myocytes [60–63].

DOI: 10.1002/nme

with experimental observations for similar conditions (the insets of Figure 10g–i) [60–63]. Here, our results show that SFs are preferably generated in directions of maximum apparent stiffness, corresponding to lines connecting adhesion islands. This can be explained as follows. In directions of maximum stiffness, the constraints on tensile deformation result in a decreased strain rate, which, according to the Hill model, results in optimal contraction (Figure 4). Because SF formation increases with contraction (Equation (16)), this explains the high density of SFs along directions of high apparent stiffness. This type of simulation is critical to interpreting a variety of experimental procedures that can measure mechanical forces and deformation with arrays of micropillars or elastic gels in which fluorescent beads are embedded [33, 64, 65]. Furthermore, Figure 10d and f shows that the first invariant of substrate stress under square and rectangular cells agrees very well with the ordinary FEM results except for the corners where the reason is that focal adhesions are applied to nodes in the ordinary FEM. The same good agreement is observed in Figure 10g and i for distribution and orientation of SF in the same cells.

5.3. *Effect of substrate's stiffness on cell contraction and deformation*

Experimental studies have shown that cell contraction and SF structure are strongly influenced by the stiffness of the underlying matrix [66–69]. Here, we propose to assess how the proposed model captures these effects and compare the XFEM predictions with ordinary FEM results. For this, we consider the square cell shown in Figure 10a, adhering to a substrate of varying stiffness through focal adhesions located at its corners. Similar to previous examples, initial conditions are such that no SFs are present at $t = 0$, and the substrate is subjected to periodic boundary conditions. To assess the magnitude of cell contraction, we computed the normalized average tensile force in focal adhesions $F/(\bar{T}\ d^2)$ when the steady state was reached (here, d is the typical dimension of the cell). This quantity was computed for values of normalized substrate's stiffness E^s/E^c ranging from 0 to 300, which led to the nonlinear contraction–stiffness relationship depicted in Figure 11. The result of Figure 11 can generally be explained by the fact that increasing substrate stiffness tends to decrease the strain rates undergone by SF and thus increase contraction (according to Hill's model). This increased contraction subsequently promotes more SF formation, which leads to a rise in SF density and contraction. The time evolution of contraction is also shown in the inset of Figure 11 in terms of the normalized time $t^\star = t\dot{\varepsilon}_0$ for the case $E^s = 1000$ Pa. The simulation was performed using the XFEM (with a single mesh) and the ordinary FEM (using different meshes for cell and substrate) with the same element size. As expected, we observed a very good agreement between the two approaches. The slightly higher contractile force predicted by the XFEM may, once again, be attributed to the differences in handling corner regions and cell–substrate adhesion between the two methods.

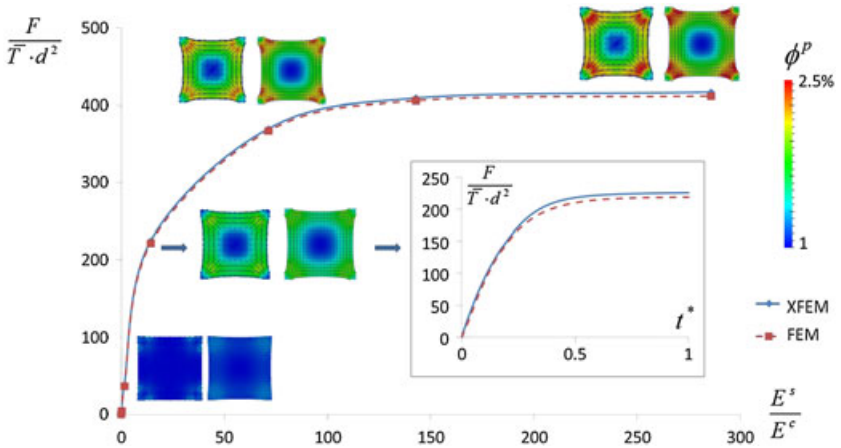

Figure 11. Changes of the normalized force applied to the substrate by the cell in an adhesion island as a function of normalized substrate's stiffness and normalized time, together with the volume fraction and orientation of stress fibers generated in the cell and comparison between the FEM and the extended FEM (XFEM).

DOI: 10.1002/nme

A relevant question in biology is to understand how the mechanical work performed by cells is affected by the stiffness of the substrate they lie on. Here, we assess the average mechanical work of a cell as $W = Fd$, where F is the average force it applies to its focal adhesion and d is the resulting average displacement. Figure 12 shows the changes of work W as the relative substrate's stiffness varies from 0 to 1000 as predicted by the XFEM and the FEM. The figure clearly shows very good agreement between the two methods. Physically, the figure shows that no mechanical work is performed for small and large values of substrate stiffness; indeed, small stiffness results in no contraction (Figure 11), whereas large stiffness precludes substrate deformation. A consequence is that there exists an optimal substrate stiffness for which the work performed by cells is maximum (with our parameters, this optimum occurs in the range of $10E_c < E_s < 30E_c$), a phenomenon that has been observed experimentally for cardiomyocytes by Engler *et al.* [64]. This result therefore illustrates why such simulation can be essential for the choice of artificial gels with optimal mechanical properties in the context of tissue engineering.

5.4. *Effect of cortical stiffness on cell contraction*

In the last example, we propose to investigate the influence of cortical stiffness on the evolution of SF and cell contraction [9, 15]. We concentrated on the particular case of a square cell lying on a substrate whose stiffness is $E_s = 1000E_c$. The geometry and numerical discretization for this problem are displayed in the previous example. If we define $T^0 = G \cdot \bar{T}$, where G denotes the average SF volume fraction in the cell according to Equation (52), the normalized cortex stiffness $E_\sigma/(T^0 d)$ is then varied from 0 to 10,000, and the steady-state SF distribution is evaluated for various cases. As discussed in [9] and [15], the existence of a stiff cortical layer around a cell tends to homogenize membrane curvature. This effect is nicely captured by the graph of Figure 13 that shows the decreasing average cortex curvature d/R with increasing cortical stiffness. To assess the accuracy of the prediction of the XFEM, the numerical results are compared with the analytical solution [9] given by the following:

$$\frac{1}{\frac{1}{R}\cdot d} = \frac{E_\sigma}{T^0 d}\left(\frac{2}{\frac{1}{R}\cdot d}\ \arcsin\left(\frac{\frac{1}{R}\cdot d}{2}\right) - 1\right). \tag{55}$$

Note that the preceding expression is computed on the basis of the Laplace law and by assuming that the contractile stress T^0 is applied in a direction normal to the cell membrane. It can therefore be interpreted as a negative pressure in the cell and the effects of Poisson's ratio and cell's body Young's modulus are not taken into account. As a result, for small values of the cortex stiffness E_σ, the properties of the internal cell's cytoskeleton control cortex curvature, and the analytical solution

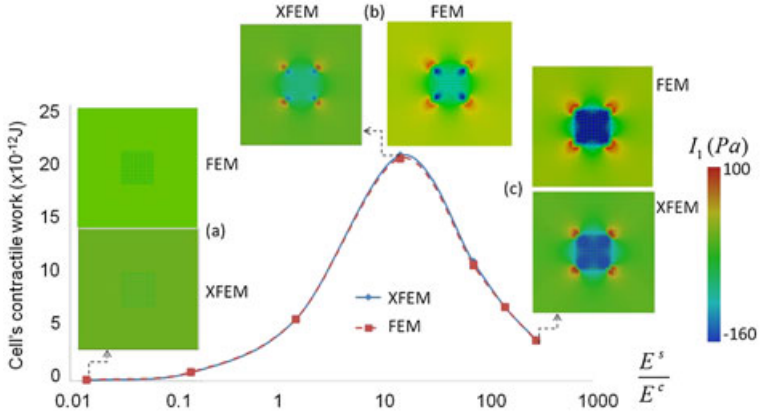

Figure 12. The changes of the work carried out by focal adhesion force on the cell with substrate's stiffness; and the substrate's first invariant of stress tensor I_1 for different substrates' Young's modulus and comparison with ordinary FEM: (a) $E^s = 1$ Pa, (b) $E^s = 1000$ Pa, (c) $E^s = 20{,}000$ Pa.

DOI: 10.1002/nme

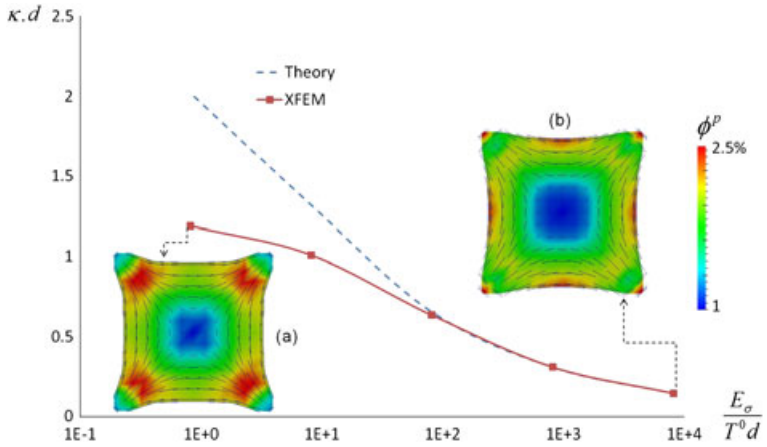

Figure 13. The effect of cortex stiffness on its curvature and stress fiber formation and comparison of cortex curvature with analytical solution carried out in Reference [9]. (a) $E_\sigma = 0$, (b)$E_\sigma = 10$ N/m.

loses its validity. However, for large values of E_σ, the cortical stiffness dominates, and the numerical results converge to the analytical solution. This result therefore provides an excellent measure of the accuracy of the XFEM in capturing the effect of the cortex on the overall cell deformation. On another note, our simulation also shows that the effect of cortical stiffness on SF generation is significant. Indeed, Figure 13 shows that SFs tend to increasingly align in parallel with the cortex as cortical stiffness increases. The reason is clear: increasing cortical stiffness results in rising stiffness in directions that are tangential to the cell membrane. As the model predicts SF formation in directions of maximum stiffness, more SFs are generated near and in parallel to the membrane. These results have been confirmed by a previous study [70], showing that the existence of a constrained boundary leads to generation of SF along the boundary.

6. SUMMARY AND CONCLUDING REMARKS

In summary, this paper presented a numerical approach to study the behavior of contractile cells and their interactions with a two-dimensional elastic substrate. The continuum model of cell contraction is based on a constrained mixture formulation [14] that describes the contractile apparatus of cells in terms of four major constituents, namely cytoskeleton, cytosol, G-actin monomers, and F-actin (or SF) polymers. This framework enables us to characterize important processes of cell contraction such as SF formation (mass exchange between actin monomers and SF), actin diffusion, and convection as well as the evolution of an anisotropic contractile network in time. Biologically, the model rests on two key assumptions: (1) SF contraction increases with decreasing strain rate (Hill's model) and (2) SF formation is promoted by contraction. The interactions of cells with their underlying substrate were then considered through focal adhesions, modeled here by an elastic cohesive law between the two continua.

The main contribution of this work was the introduction of an XFEM–level set approach to accurately and efficiently model the interactions between cells of arbitrary shapes and an underlying deformable substrate. The key features of the proposed method are as follows:

- Despite being represented by two distinct domains, cell and substrate are discretized by a single regular finite element mesh. The (possibly complex) cell geometry is then defined in terms of an analytical function (the level set function) that is independent of discretization. This feature has the merit of greatly simplifying the numerical issues associated with meshing complex geometries and handling interactions between bodies discretized by distinct meshes.
- The stiffness of the thin cortical layer surrounding cells can naturally be accounted for by incorporating surface elasticity on the cell boundary. This feature is possible by enriching the XFEM shape functions with weak discontinuity functions, which enables a jump in stress across the cell membrane.

DOI: 10.1002/nme

- Because cell geometry is independent of discretization, the method can be extended to describe cell growth, migration, and spreading without resorting to remeshing techniques, known to be computationally expensive. Instead, more efficient techniques involving level set evolution equations can be invoked. This will be the object of future studies.

The performance of the method was then assessed by considering biologically relevant problems of cell–substrate interactions. Generally, our results showed that the proposed numerical method, together with the constrained mixture formulation, led to realistic behaviors that correlated very well with ordinary FEM and experimental observations. The coupling of the XFEM and the level set approach therefore provides a promising route to study a variety of biological problems involving cell–substrate interactions, such as morphogenesis, tissue engineering, cell spreading, and migration as well as wound contraction.

APPENDIX A: GOVERNING EQUATIONS FOR PLANE STRESS ASSUMPTIONS

As mentioned previously, both cell and substrate are considered in 2D x–y plane stress because of small thickness for the cell and simplicity for the substrate. For substrate as a homogeneous material, it is assumed that $T^{\mathrm{s}}_{zz} = T^{\mathrm{s}}_{xz} = T^{\mathrm{s}}_{yz} = 0$, where T^{s} is substrate's Cauchy stress. The details of 2D plane stress condition for a solid can be found in any mechanic of materials book. But the condition of plane stress for cell as a mixture is different because of the existence of the fluid phase and is written as $T_{xz} = T_{yz} = 0$, $T_{zz} - p = 0$, or $T^{\sigma J}_{xz} = T^{\sigma J}_{yz} = 0$, $T^{\sigma J}_{zz} - \dot{p} = 0$. To find the stress–strain relationship for this situation, one can start from the general material rate form of stress–strain relationship written in Voigt notation as [52]

$$\begin{bmatrix} T^{\sigma J}_{xx} \\ T^{\sigma J}_{yy} \\ T^{\sigma J}_{zz} \\ T^{\sigma J}_{yz} \\ T^{\sigma J}_{xz} \\ T^{\sigma J}_{xy} \end{bmatrix} = \begin{bmatrix} 2\mu'+\lambda & \lambda & \lambda & 0 & 0 & 0 \\ \lambda & 2\mu'+\lambda & \lambda & 0 & 0 & 0 \\ \lambda & \lambda & 2\mu'+\lambda & 0 & 0 & 0 \\ 0 & 0 & 0 & \mu' & 0 & 0 \\ 0 & 0 & 0 & 0 & \mu' & 0 \\ 0 & 0 & 0 & 0 & 0 & \mu' \end{bmatrix} \begin{bmatrix} D_{xx} \\ D_{yy} \\ D_{zz} \\ 2D_{yz} \\ 2D_{xz} \\ 2D_{xy} \end{bmatrix}, \tag{A.1}$$

where $\mu' = \mu - \lambda \ln J$. Then, by applying the plane stress conditions to the preceding equation, we can easily derive the equation

$$D_{zz} = \frac{1}{1-\nu}\left[\frac{p}{E}(1+\nu)(1-2\nu) - \nu(D_{xx}+D_{yy})\right], \tag{A.2}$$

where E and ν are cytoskeleton's Young's modulus and Poisson's ratio, respectively, and are given by

$$E = \frac{\mu'(3\lambda+2\mu')}{\lambda+\mu'} \quad \text{and} \quad \nu = \frac{\lambda}{2(\lambda+\mu')}. \tag{A.3}$$

Consequently, the Jaumann rate of cytoskeleton Cauchy stress is written as

$$\begin{bmatrix} T^{\sigma J}_{xx} \\ T^{\sigma J}_{yy} \\ T^{\sigma J}_{xy} \end{bmatrix} = \frac{E}{(1-\nu^2)} \begin{bmatrix} 1 & \nu & 0 \\ \nu & 1 & 0 \\ 0 & 0 & \frac{1-\nu}{2} \end{bmatrix} \begin{bmatrix} D_{xx} \\ D_{yy} \\ 2D_{xy} \end{bmatrix} + \frac{\nu}{1-\nu} p \begin{bmatrix} 1 \\ 1 \\ 0 \end{bmatrix}. \tag{A.4}$$

Equation (A.4) is written in matrix notation in the x–y plane as $\mathbf{T}^{\sigma J} = \mathbf{C}^{\mathrm{c}} : \mathbf{D} + (\nu/1-\nu)p\mathbf{I}$. Furthermore, with the use of Equation (A.2) and the 3D divergence of cytoskeleton velocity $\nabla^{(3)}\cdot\mathbf{v} = D_{xx} + D_{yy} + D_{zz}$, it is concluded that $\nabla^{(3)}\cdot\mathbf{v} = \alpha\,\nabla\cdot\mathbf{v} + \beta\,\dot{p}$, where $\nabla\cdot\mathbf{v} = D_{xx} + D_{yy}$ introduces 2D divergence of velocity and the constants α and β are given as a function of cytoskeleton's material properties (Young's modulus and Poisson's ratio) given by the following:

$$\alpha = \frac{1-2\nu}{1-\nu} \quad \text{and} \quad \beta = \frac{(1+\nu)(1-2\nu)}{E(1-\nu)}. \tag{A.5}$$

DOI: 10.1002/nme

APPENDIX B: INCREMENTAL WEAK FORM OF THE GOVERNED EQUATIONS

Before writing the incremental form of the set of derived equations, we need to find equations for $\delta\phi^{\mathrm{f}}$ and $\dot{\phi}^{\mathrm{f}} = D\phi^{\mathrm{f}}/Dt$ as a function of cell's variables. As mentioned before, cell's body is assumed to be saturated by four constituents: cytoskeletal network, cytosol, SF polymers, and G-actin monomers; consequently, one can write $\phi^{\mathrm{f}} + \phi^{\mathrm{c}} + \phi^{\mathrm{p}} + \phi^{\mathrm{m}} = 1$. After deriving the material time derivative of the latter equation, we obtain the formula $\dot{\phi}^{\mathrm{f}} = \dot{\phi}^{\mathrm{c}} - \dot{\phi}^{\mathrm{p}} - \dot{\phi}^{\mathrm{m}}$, where ϕ denotes the volume fraction of each cell's component and the superscripts f, c, p, and m stand for cytosol, cytoskeleton, polymers, and monomers, respectively. Furthermore, following [14] and considering plane stress condition for the cell, the balance of mass equation for cytoskeleton takes the following form: $D\phi^{\mathrm{c}}/Dt = \dot{\phi}^{\mathrm{c}} = -\phi^{\mathrm{c}}\ \alpha\ \nabla\cdot\dot{\mathbf{u}} - \phi^{\mathrm{c}}\ \beta\ \dot{p}$.

As a result,

$$\begin{cases} \dot{\phi}^{\mathrm{f}} = \phi^{\mathrm{c}}\ \alpha\ \nabla\cdot\dot{\mathbf{u}} + \phi^{\mathrm{c}}\ \beta\ \dot{p} - \mathrm{tr}\left(\dot{\mathbf{\Phi}}^{\mathrm{p}}\right) - \dot{\phi}^{\mathrm{m}} \\ \delta\phi^{\mathrm{f}} = \phi^{\mathrm{c}}\ \alpha\ \nabla\cdot\delta\mathbf{u} + \phi^{\mathrm{c}}\ \beta\ \delta p - \mathrm{tr}\left(\delta\mathbf{\Phi}^{\mathrm{p}}\right) - \delta\phi^{\mathrm{m}} \end{cases}. \tag{B.1}$$

To write the nonlinear form, the Jaumann rate is used for Cauchy stress values because of large deformations of cell and substrate [52]. As a result, the nonlinear equations take the following forms:

$$\begin{aligned} \int_{\Omega^{\mathrm{s}}} \nabla\boldsymbol{\omega}^{\mathrm{s}} : \left[\tilde{\mathbf{T}}^{\mathrm{s}} + \left(\mathbf{C}^{\mathrm{s}} : \mathbf{D}^{\mathrm{s}} + \mathbf{W}^{\mathrm{s}}\cdot\tilde{\mathbf{T}}^{\mathrm{s}} + \tilde{\mathbf{T}}^{\mathrm{s}}\cdot\mathbf{W}^{\mathrm{s}\mathrm{T}}\right)\cdot\delta t\right]\,\mathrm{d}\Omega^{\mathrm{s}} \\ - \int_{\Omega^{\mathrm{c}}} \boldsymbol{\omega}^{\mathrm{s}}\cdot\left[\,\tilde{\mathbf{t}}_{\mathrm{a}} + \mathbf{K}_{\mathrm{a}}\left(\mathbf{v}^{\mathrm{c}} - \mathbf{v}^{\mathrm{s}}\right)\cdot\delta t\right]\,\mathrm{d}\Omega^{\mathrm{c}} = 0, \end{aligned} \tag{B.2}$$

$$\begin{aligned} \int_{\Omega^{\mathrm{c}}} \nabla\boldsymbol{\omega} : \Bigg[& \left(\tilde{\mathbf{T}}^{\mathrm{c}} + \tilde{\mathbf{T}}^{\mathrm{p}} - \tilde{p}\ \mathbf{I}\right) + \left(\mathbf{C}^{\mathrm{c}} : \mathbf{D} + \left(\frac{\nu}{1-\nu}\right)\dot{p}\mathbf{I} + \mathbf{W}\cdot\tilde{\mathbf{T}}^{\mathrm{c}} + \tilde{\mathbf{T}}^{\mathrm{c}}\cdot\mathbf{W}^{\mathrm{T}}\right)\cdot\delta t \\ & + \frac{\partial\mathbf{T}^{\mathrm{p}}}{\partial\mathbf{\Phi}^{\mathrm{p}}} : \delta\mathbf{\Phi}^{\mathrm{p}} + \frac{\partial\mathbf{T}^{\mathrm{p}}}{\partial\mathbf{E}} : \delta\mathbf{E} + \frac{\partial\mathbf{T}^{\mathrm{p}}}{\partial\dot{\mathbf{E}}} : \delta\dot{\mathbf{E}} + \left(\mathbf{W}\cdot\tilde{\mathbf{T}}^{\mathrm{p}} + \tilde{\mathbf{T}}^{\mathrm{p}}\cdot\mathbf{W}^{\mathrm{T}}\right)\cdot\delta t - \delta p\ \mathbf{I}\Bigg]\,\mathrm{d}\Omega^{\mathrm{c}} \\ & + \int_{\Omega^{\mathrm{d}}} \boldsymbol{\omega}\cdot\left[\,\tilde{\mathbf{t}}_{\mathrm{a}} + \mathbf{K}_{\mathrm{a}}\left(\mathbf{v}^{\mathrm{c}} - \mathbf{v}^{\mathrm{s}}\right)\cdot\delta t\right]\,\mathrm{d}\Omega^{\mathrm{d}} \\ & + \int_{\Gamma^{\mathrm{c}}} \left(\mathbf{P}\cdot\nabla\boldsymbol{\omega}\cdot\mathbf{P}\right) : \left[\tilde{\mathbf{T}}_{\sigma} + \left(\mathbf{S}_{\sigma} : \mathbf{D}_{\sigma} + \mathbf{W}_{\sigma}\cdot\tilde{\mathbf{T}}_{\sigma} + \tilde{\mathbf{T}}_{\sigma}\cdot\mathbf{W}_{\sigma}^{\mathrm{T}}\right)\cdot\delta t\right]\,\mathrm{d}\Gamma^{\mathrm{c}} = 0, \end{aligned} \tag{B.3}$$

$$\begin{aligned} & \int_{\Omega^{\mathrm{c}}} \theta\ \left[\,\alpha\ \nabla\cdot\mathbf{v} + \ \beta\ \dot{p}\right]\,\mathrm{d}\Omega^{\mathrm{c}} \\ & + \int_{\Omega^{\mathrm{c}}} \nabla\theta\cdot\Bigg[\frac{\kappa}{\mu}\nabla\tilde{p} + \left(\frac{\tilde{\phi}^{\mathrm{m}}}{\tilde{\phi}^{\mathrm{f}}}\frac{\kappa}{\mu}\nabla\tilde{p} + D\ \nabla\tilde{\phi}^{\mathrm{m}} - \frac{\tilde{\phi}^{\mathrm{m}}}{\tilde{\phi}^{\mathrm{f}}}D\ \nabla\tilde{\phi}^{\mathrm{f}}\right) \\ & \qquad + \frac{\kappa}{\mu}\nabla\delta p + \left(\frac{\delta\phi^{\mathrm{m}}}{\tilde{\phi}^{\mathrm{f}}}\frac{\kappa}{\mu}\nabla\tilde{p} + \frac{\tilde{\phi}^{\mathrm{m}}}{\tilde{\phi}^{\mathrm{f}}}\frac{\kappa}{\mu}\nabla\delta p + D\ \nabla\delta\phi^{\mathrm{m}} - \frac{\delta\phi^{\mathrm{m}}}{\tilde{\phi}^{\mathrm{f}}}D\ \nabla\tilde{\phi}^{\mathrm{f}}\right) \\ & \qquad + \frac{\tilde{\phi}^{\mathrm{m}}}{\tilde{\phi}^{\mathrm{f}}}\left(-\frac{1}{\tilde{\phi}^{\mathrm{f}}}\frac{\kappa}{\mu}\nabla\tilde{p} + \frac{1}{\tilde{\phi}^{\mathrm{f}}}D\ \nabla\tilde{\phi}^{\mathrm{f}}\right)\cdot\left(\tilde{\phi}^{\mathrm{c}}\ \alpha\ \nabla\cdot\delta\mathbf{u} + \tilde{\phi}^{\mathrm{c}}\ \beta\ \delta p - \mathrm{tr}\left(\delta\mathbf{\Phi}^{\mathrm{p}}\right) - \delta\phi^{\mathrm{m}}\right) \\ & \qquad - \frac{\tilde{\phi}^{\mathrm{m}}}{\tilde{\phi}^{\mathrm{f}}}D\ \nabla\left(\tilde{\phi}^{\mathrm{c}}\ \alpha\ \nabla\cdot\delta\mathbf{u} + \tilde{\phi}^{\mathrm{c}}\ \beta\ \delta p - \mathrm{tr}\left(\delta\mathbf{\Phi}^{\mathrm{p}}\right) - \delta\phi^{\mathrm{m}}\right)\Bigg]\,\mathrm{d}\Omega^{\mathrm{c}} = 0, \end{aligned} \tag{B.4}$$

$$\begin{aligned} \int_{\Omega^{\mathrm{c}}} \lambda\Big[& \left(\tilde{\phi}^{\mathrm{c}}\ \alpha\ \nabla\cdot\dot{\mathbf{u}} + \tilde{\phi}^{\mathrm{c}}\ \beta\ \dot{p} - \mathrm{tr}\left(\dot{\mathbf{\Phi}}^{\mathrm{p}}\right) - \dot{\phi}^{\mathrm{m}}\right) \\ & + \tilde{\phi}^{\mathrm{f}}\ \left(\ \alpha\ \nabla\cdot\dot{\mathbf{u}} + \ \beta\ \dot{p}\right)\Big]\,\mathrm{d}\Omega^{\mathrm{c}} + \int_{\Omega^{\mathrm{c}}} \nabla\lambda\cdot\left(\frac{\kappa}{\mu}\nabla\tilde{p} + \frac{\kappa}{\mu}\nabla\delta p\right)\,\mathrm{d}\Omega^{\mathrm{c}} = 0, \end{aligned} \tag{B.5}$$

DOI: 10.1002/nme

$$\int_{\Omega^{\mathrm{c}}} \mathbf{\Lambda} : \Bigg[\dot{\mathbf{\Phi}}^{\mathrm{p}} + \tilde{\mathbf{\Phi}}^{\mathrm{p}} \left(\alpha \, \nabla \cdot \mathbf{v} + \beta \, \dot{p} \right) - \left(\frac{M^{\mathrm{p}}}{M^{\mathrm{m}}} \left(\frac{1}{2} k_0^{\mathrm{f}} \mathbf{I} + k_1^{\mathrm{f}} \tilde{\mathbf{T}}^{\mathrm{p}} \right) \frac{\tilde{\phi}^{\mathrm{m}}}{\tilde{\phi}^{\mathrm{f}}} - k_0^{\mathrm{d}} \tilde{\mathbf{\Phi}}^{\mathrm{p}} \right)$$
$$- \left(\frac{M^{\mathrm{p}}}{M^{\mathrm{m}}} k_1^{\mathrm{f}} \left(\frac{\partial \mathbf{T}^{\mathrm{p}}}{\partial \mathbf{\Phi}^{\mathrm{p}}} : \delta \mathbf{\Phi}^{\mathrm{p}} + \frac{\partial \mathbf{T}^{\mathrm{p}}}{\partial \mathbf{E}} : \delta \mathbf{E} + \frac{\partial \mathbf{T}^{\mathrm{p}}}{\partial \dot{\mathbf{E}}} : \delta \dot{\mathbf{E}} \right) \frac{\tilde{\phi}^{\mathrm{m}}}{\tilde{\phi}^{\mathrm{f}}} \right.$$
$$\left. + \frac{M^{\mathrm{p}}}{M^{\mathrm{m}}} k_1^{\mathrm{f}} \left(\mathbf{W} \cdot \tilde{\mathbf{T}}^{\mathrm{p}} + \tilde{\mathbf{T}}^{\mathrm{p}} \cdot \mathbf{W}^{\mathrm{T}} \right) \frac{\tilde{\phi}^{\mathrm{m}}}{\tilde{\phi}^{\mathrm{f}}} \right) \tag{B.6}$$
$$- \left(\frac{M^{\mathrm{p}}}{M^{\mathrm{m}}} \left(\frac{1}{2} k_0^{\mathrm{f}} \mathbf{I} + k_1^{\mathrm{f}} \tilde{\mathbf{T}}^{\mathrm{p}} \right) \frac{\delta \phi^{\mathrm{m}}}{\tilde{\phi}^{\mathrm{f}}} - k_0^{\mathrm{d}} \, \delta \mathbf{\Phi}^{\mathrm{p}} \right) - \frac{M^{\mathrm{p}}}{M^{\mathrm{m}}} \left(\frac{1}{2} k_0^{\mathrm{f}} \mathbf{I} + k_1^{\mathrm{f}} \tilde{\mathbf{T}}^{\mathrm{p}} \right) \frac{-\tilde{\phi}^{\mathrm{m}}}{\tilde{\phi}^{\mathrm{f}^2}}$$
$$\cdot \left(\tilde{\phi}^{\mathrm{c}} \, \alpha \, \nabla \cdot \delta \mathbf{u} + \tilde{\phi}^{\mathrm{c}} \, \beta \, \delta p - \mathrm{tr} \left(\delta \mathbf{\Phi}^{\mathrm{p}} \right) - \delta \phi^{\mathrm{m}} \right) \Bigg] \, \mathrm{d}\Omega^{\mathrm{c}} = 0.$$

APPENDIX C: DISCRETIZED FORM OF THE GOVERNED EQUATIONS

To discretize the equations derived formerly, Voigt notation is used for all symmetric tensors. In Voigt notation, all stress and strain tensors are written as

$$\{\mathbf{T}\} = \begin{bmatrix} T_{11} \\ T_{22} \\ T_{12} \end{bmatrix}; \quad \{\mathbf{E}\} = \begin{bmatrix} E_{11} \\ E_{22} \\ 2\, E_{12} \end{bmatrix}; \quad \{\mathbf{D}\} = \begin{bmatrix} D_{11} \\ D_{22} \\ 2\, D_{12} \end{bmatrix}; \quad \{\mathbf{W}\} = \begin{bmatrix} W_{11} \\ W_{22} \\ 2\, W_{12} \end{bmatrix}. \tag{C.1}$$

For structural matrix, we use

$$\{\mathbf{\Phi}^{\mathrm{p}}\} = \begin{bmatrix} \phi_{11}^{\mathrm{p}} \\ \phi_{22}^{\mathrm{p}} \\ \phi_{12}^{\mathrm{p}} \end{bmatrix}. \tag{C.2}$$

Also, we make the definitions

$$\mathbf{W} \cdot \mathbf{T} + \mathbf{T} \cdot \mathbf{W}^{\mathrm{T}} \equiv \{\{\mathbf{T}\}\} \cdot \mathbf{G} \cdot \dot{\mathbf{u}}^{e}, \tag{C.3}$$

$$\delta \mathbf{W} \cdot \mathbf{T} + \mathbf{T} \cdot \delta \mathbf{W}^{\mathrm{T}} \equiv \{\{\mathbf{T}\}\} \cdot \mathbf{G} \cdot \delta \mathbf{u}^{e}, \tag{C.4}$$

where

$$\{\{\mathbf{T}\}\} = \begin{bmatrix} 2\, T_{12} \\ -2\, T_{12} \\ T_{22} - T_{11} \end{bmatrix}, \tag{C.5}$$

$$\mathbf{G} = \begin{bmatrix} \mathbf{G}_1 & \mathbf{G}_2 & \ldots & \mathbf{G}_{9+m} \end{bmatrix} \text{ and } \mathbf{G}_I = 0.5 \begin{bmatrix} \frac{\partial N_I(\mathbf{x})}{\partial x_2} & -\frac{\partial N_I(\mathbf{x})}{\partial x_1} \end{bmatrix}, \tag{C.6}$$

for substrate

$$\mathbf{G}^{\mathrm{s}} = \begin{bmatrix} \mathbf{G}_1 & \mathbf{G}_2 & \ldots & \mathbf{G}_9 \end{bmatrix}. \tag{C.7}$$

In this paper, quadratic nine-node (commonly called Q9) elements are used for displacement fields $\mathbf{u}^{\mathrm{s}}$ and $\mathbf{u}$, whereas for the other three fields (p, ϕ^{m}, and $\mathbf{\Phi}^{\mathrm{p}}$), quadratic four-node (commonly called Q4) elements are used. As a result, the parameter n in Equation (42) is 9 for displacement fields and 4 for the other fields.

DOI: 10.1002/nme

Furthermore, the following definitions will be used for discretization:

$$\boldsymbol{\omega}^{\mathrm{s}} = \mathbf{N}^{\mathrm{s}} \cdot \boldsymbol{\omega}^{\mathrm{s},e};\ \ \boldsymbol{\omega} = \mathbf{N} \cdot \boldsymbol{\omega}^{e};\ \ \theta = \mathbf{N}_{\mathrm{f}} \cdot \boldsymbol{\theta}^{e};\ \ \lambda = \mathbf{N}_{\mathrm{f}} \cdot \boldsymbol{\lambda}^{e};\ \ \boldsymbol{\Lambda} = \mathbf{N}_{\mathrm{p}} \cdot \boldsymbol{\Lambda}^{e}, \tag{C.8}$$

$$\mathbf{u}^{\mathrm{s}} = \mathbf{N}^{\mathrm{s}} \cdot \mathbf{u}^{\mathrm{s},e};\ \ \mathbf{u} = \mathbf{N} \cdot \mathbf{u}^{e};\ \ p = \mathbf{N}_{\mathrm{f}} \cdot \mathbf{p}^{e};\ \ \phi^{\mathrm{m}} = \mathbf{N}_{\mathrm{f}} \cdot \boldsymbol{\Phi}^{\mathrm{m},e};\ \ \boldsymbol{\Phi}^{\mathrm{p}} = \mathbf{N}_{\mathrm{p}} \boldsymbol{\Phi}^{\mathrm{p},e}, \tag{C.9}$$

$$\nabla \boldsymbol{\omega}^{\mathrm{s}} = \mathbf{B}^{\mathrm{s}} \cdot \boldsymbol{\omega}^{\mathrm{s},e};\ \ \nabla \boldsymbol{\omega} = \mathbf{B} \cdot \boldsymbol{\omega}^{e};\ \ \nabla \theta = \mathbf{B}_{\mathrm{f}} \cdot \boldsymbol{\theta}^{e};\ \ \nabla \lambda = \mathbf{B}_{\mathrm{f}} \cdot \boldsymbol{\lambda}^{e}, \tag{C.10}$$

$$\nabla \mathbf{u}^{\mathrm{s}} = \mathbf{B}^{\mathrm{s}} \cdot \mathbf{u}^{\mathrm{s},e};\ \ \nabla \mathbf{u} = \mathbf{B} \cdot \mathbf{u}^{e};\ \ \nabla p = \mathbf{B}_{\mathrm{f}} \cdot \mathbf{p}^{e};\ \ \nabla \phi^{\mathrm{m}} = \mathbf{B}_{\mathrm{f}} \cdot \boldsymbol{\Phi}^{\mathrm{m},e}, \tag{C.11}$$

$$\nabla \cdot \mathbf{u} = \tilde{\mathbf{B}} \cdot \mathbf{u}^{e};\ \ \{\mathbf{D}\} = \mathbf{B} \cdot \dot{\mathbf{u}}^{e};\ \ \{\mathbf{D}^{s}\} = \mathbf{B}^{\mathrm{s}} \cdot \dot{\mathbf{u}}^{\mathrm{s},e}. \tag{C.12}$$

The same definitions are used for rates. In preceding equations, if it is assumed that m and m' are the number of enriched nodes in Q9 and Q4 elements, respectively, the following definitions are given,

$$\mathbf{N}^{\mathrm{s}} = \begin{bmatrix} \mathbf{N}^1 & \mathbf{N}^2 & \cdots & \mathbf{N}^9 \end{bmatrix};\ \ \mathbf{N} = \begin{bmatrix} \mathbf{N}^1 & \mathbf{N}^2 & \cdots & \mathbf{N}^{9+m} \end{bmatrix};\ \ \mathbf{N}^I = \begin{bmatrix} N^I & 0 \\ 0 & N^I \end{bmatrix}, \tag{C.13}$$

$$\mathbf{N}_{\mathrm{f}} = \begin{bmatrix} M^1 & M^2 & \cdots & M^{4+m'} \end{bmatrix}, \tag{C.14}$$

$$\mathbf{N}_{\mathrm{p}} = \begin{bmatrix} \mathbf{N}^1 & \mathbf{N}^2 & \cdots & \mathbf{N}^{4+m'} \end{bmatrix};\ \ \mathbf{N}^I = \begin{bmatrix} M^I & 0 & 0 \\ 0 & M^I & 0 \\ 0 & 0 & M^I \end{bmatrix}, \tag{C.15}$$

where N^I and M^I are quadrature nine-node and four-node shape functions, respectively. Also,

$$\mathbf{B}^{\mathrm{s}} = \begin{bmatrix} \mathbf{B}^1 & \mathbf{B}^2 & \cdots & \mathbf{B}^9 \end{bmatrix};\ \ \mathbf{B} = \begin{bmatrix} \mathbf{B}^1 & \mathbf{B}^2 & \cdots & \mathbf{B}^{9+m} \end{bmatrix};\ \ \mathbf{B}^I = \begin{bmatrix} \frac{\partial N^I}{\partial x_1} & 0 \\ 0 & \frac{\partial N^I}{\partial x_2} \\ \frac{\partial N^I}{\partial x_2} & \frac{\partial N^I}{\partial x_1} \end{bmatrix}, \tag{C.16}$$

$$\tilde{\mathbf{B}} = \begin{bmatrix} \tilde{\mathbf{B}}^1 & \tilde{\mathbf{B}}^2 & \cdots & \tilde{\mathbf{B}}^{9+m} \end{bmatrix};\ \ \tilde{\mathbf{B}}^I = \begin{bmatrix} \frac{\partial N^I}{\partial x_1} & \frac{\partial N^I}{\partial x_2} \end{bmatrix}, \tag{C.17}$$

$$\mathbf{B}_{\mathrm{f}} = \begin{bmatrix} \mathbf{B}_{\mathrm{f}}^1 & \mathbf{B}_{\mathrm{f}}^2 & \cdots & \mathbf{B}_{\mathrm{f}}^{4+m'} \end{bmatrix};\ \ \mathbf{B}_{\mathrm{f}}^I = \begin{bmatrix} \frac{\partial M^I}{\partial x_1} & \frac{\partial M^I}{\partial x_2} \end{bmatrix}^{\mathrm{T}}. \tag{C.18}$$

Furthermore, knowing that, in matrix notation, $\dot{\mathbf{E}} = \mathbf{F}^{\mathrm{T}} \cdot \mathbf{D} \cdot \mathbf{F}$, $\mathbf{F}^m$ is chosen such that, in Voigt notation, one can write $\{\dot{\mathbf{E}}\} = \mathbf{F}^m \cdot \{\mathbf{D}\}$, where

$$\mathbf{F}^m = \begin{bmatrix} F_{11}^2 & F_{21}^2 & F_{11}\ F_{21} \\ F_{12}^2 & F_{22}^2 & F_{12}\ F_{22} \\ 2\ F_{11}\ F_{12} & 2\ F_{21}\ F_{22} & F_{11}\ F_{22} + F_{12}\ F_{21} \end{bmatrix}. \tag{C.19}$$

As a result, the discretized nonlinear weak form of Equations (B.2)–(B.6) takes the following forms:

$$\begin{aligned} \boldsymbol{\omega}^{\mathrm{s},e\mathrm{T}} \int_{\Omega^{\mathrm{s},e}} \mathbf{B}^{\mathrm{s}\mathrm{T}} \cdot \left(\{\tilde{\mathbf{T}}^{\mathrm{s}}\} + \{\mathbf{C}^{\mathrm{s}}\} \cdot \mathbf{B}^{\mathrm{s}} \cdot \delta \mathbf{u}^{\mathrm{s},e} + \{\{\mathbf{T}^{\mathrm{s}}\}\} \cdot \mathbf{G}^{\mathrm{s}} \cdot \delta \mathbf{u}^{\mathrm{s},e} \right) \mathrm{d}\Omega^{\mathrm{s},e} \\ - \boldsymbol{\omega}^{\mathrm{s},e\mathrm{T}} \int_{\Omega^{\mathrm{c},e}} \mathbf{N}^{\mathrm{s}\mathrm{T}} \cdot \left[\tilde{\mathbf{t}}_{\mathrm{a}} + \mathbf{K}_{\mathrm{a}} \cdot (\mathbf{N} \cdot \delta \mathbf{u}^{e} - \mathbf{N}^{\mathrm{s}} \cdot \delta \mathbf{u}^{\mathrm{s},e}) \right] \mathrm{d}\Omega^{\mathrm{c},e} = 0, \end{aligned} \tag{C.20}$$

DOI: 10.1002/nme

$$\boldsymbol{\omega}^{e\mathrm{T}} \int_{\Omega^{\mathrm{c},e}} \Bigg[\mathbf{B}^{\mathrm{T}} \cdot \Big(\{\tilde{\mathbf{T}}^{\mathrm{c}}\} + \{\tilde{\mathbf{T}}^{\mathrm{p}}\} + \{\mathbf{C}^{\mathrm{c}}\} \cdot \mathbf{B} \cdot \delta\mathbf{u}^{e} + \{\{\mathbf{T}^{\mathrm{c}}\}\} \cdot \mathbf{G} \cdot \delta\mathbf{u}^{e} + \frac{\{\partial \mathbf{T}^{\mathrm{p}}\}}{\{\partial \boldsymbol{\Phi}^{\mathrm{p}}\}} \cdot \mathbf{N}^{\mathrm{p}} \cdot \delta\boldsymbol{\Phi}^{\mathrm{p},e} + \frac{\partial \{\mathbf{T}^{\mathrm{p}}\}}{\partial \{\mathbf{E}\}} \cdot \mathbf{F}^{\mathrm{m}} \cdot \mathbf{B} \cdot \delta\mathbf{u}^{e} + \frac{\partial \{\mathbf{T}^{\mathrm{p}}\}}{\partial \{\dot{\mathbf{E}}\}} \cdot \mathbf{F}^{\mathrm{m}} \cdot \mathbf{B} \cdot \dot{\mathbf{u}}^{e} + \{\{\mathbf{T}^{\mathrm{p}}\}\} \cdot \mathbf{G} \cdot \delta\mathbf{u} \Big) - \tilde{\mathbf{B}}^{\mathrm{T}} \cdot \left(\tilde{p} + \frac{1-2\nu}{1-\nu} \mathbf{N}_{\mathrm{f}} \cdot \delta\mathbf{p}^{\mathrm{e}} \right) \Bigg] \mathrm{d}\Omega^{\mathrm{c},e} + \boldsymbol{\omega}^{e\mathrm{T}} \int_{\Omega^{\mathrm{c},e}} \mathbf{N}^{\mathrm{T}} \cdot \left[\tilde{\mathbf{t}}_{\mathrm{a}} + \mathbf{K}_{\mathrm{a}} \cdot (\mathbf{N} \cdot \delta\mathbf{u}^{e} - \mathbf{N}^{\mathrm{s}} \cdot \delta\mathbf{u}^{\mathrm{s},e}) \right] \mathrm{d}\Omega^{\mathrm{a}} - \boldsymbol{\omega}^{e\mathrm{T}} \int_{\sigma} \mathbf{B}^{\mathrm{T}} \cdot \mathbf{M}_{\mathrm{p}}^{\mathrm{T}} \cdot \left(\{\tilde{\mathbf{T}}_{\sigma}\} + \{\mathbf{S}^{\mathrm{s}}\} \cdot \mathbf{M}_{\mathrm{p}} \cdot \mathbf{B} \cdot \delta\mathbf{u}^{e} + \{\{\mathbf{T}_{\sigma}\}\} \cdot \mathbf{M}_{\mathrm{p}} \cdot \mathbf{G} \cdot \delta\mathbf{u}^{e} \right) \mathrm{d}\Gamma^{\mathrm{c},e} = 0, \quad \text{(C.21)}$$

$$\boldsymbol{\theta}^{e\mathrm{T}} \int_{\Omega^{\mathrm{c},e}} \mathbf{N}_{\mathrm{f}}^{\mathrm{T}} \left[\alpha\, \tilde{\mathbf{B}} \cdot \dot{\mathbf{u}}^{e} + \beta\, \mathbf{N}_{\mathrm{f}} \cdot \dot{\mathbf{p}}^{e} \right] \mathrm{d}\Omega^{\mathrm{c},e} + \boldsymbol{\theta}^{e\mathrm{T}} \int_{\Omega^{\mathrm{c},e}} \mathbf{B}_{\mathrm{f}}^{\mathrm{T}} \cdot \Bigg[\frac{\kappa}{\mu} \mathbf{B}_{\mathrm{f}} \cdot \mathbf{p}^{e} + \left(\frac{\tilde{\phi}^{\mathrm{m}}}{\tilde{\phi}^{\mathrm{f}}} \frac{\kappa}{\mu} \mathbf{B}_{\mathrm{f}} \cdot \mathbf{p}^{e} + D\, \mathbf{B}_{\mathrm{f}} \cdot \boldsymbol{\phi}^{\mathrm{m},e} - \frac{\tilde{\phi}^{\mathrm{m}}}{\tilde{\phi}^{\mathrm{f}}} D\, \nabla\tilde{\phi}^{\mathrm{f}} \right) + \frac{\kappa}{\mu} \mathbf{B}_{\mathrm{f}} \cdot \delta\mathbf{p}^{e} + \left(\frac{\mathbf{N}_{\mathrm{f}} \cdot \delta\boldsymbol{\phi}^{\mathrm{m},e}}{\tilde{\phi}^{\mathrm{f}}} \frac{\kappa}{\mu} \mathbf{B}_{\mathrm{f}} \cdot \mathbf{p}^{e} + \frac{\tilde{\phi}^{\mathrm{m}}}{\tilde{\phi}^{\mathrm{f}}} \frac{\kappa}{\mu} \mathbf{B}_{\mathrm{f}} \cdot \delta\mathbf{p}^{e} + D\, \mathbf{B}_{\mathrm{f}} \cdot \delta\boldsymbol{\phi}^{\mathrm{m},e} - \frac{\mathbf{N}_{\mathrm{f}} \cdot \delta\boldsymbol{\phi}^{\mathrm{m},e}}{\tilde{\phi}^{\mathrm{f}}} D\, \nabla\tilde{\phi}^{\mathrm{f}} \right) + \frac{\tilde{\phi}^{\mathrm{m}}}{\tilde{\phi}^{\mathrm{f}}} \left(-\frac{1}{\tilde{\phi}^{\mathrm{f}}} \frac{\kappa}{\mu} \mathbf{B}_{\mathrm{f}} \cdot \mathbf{p}^{e} + \frac{1}{\tilde{\phi}^{\mathrm{f}}} D\, \nabla\tilde{\phi}^{\mathrm{f}} \right) \cdot \left(\tilde{\phi}^{\mathrm{c}}\, \alpha\, \tilde{\mathbf{B}} \cdot \delta\mathbf{u}^{e} + \tilde{\phi}^{\mathrm{c}}\, \beta\, \mathbf{N}_{\mathrm{f}} \cdot \delta\mathbf{p}^{e} - \mathbf{m}^{\mathrm{T}} \cdot \mathbf{N}_{\mathrm{p}} \cdot \delta\boldsymbol{\Phi}^{\mathrm{p},e} - \mathbf{N}_{\mathrm{f}} \cdot \delta\boldsymbol{\phi}^{\mathrm{m},e} \right) - \frac{\tilde{\phi}^{\mathrm{m}}}{\tilde{\phi}^{\mathrm{f}}} D\, \mathbf{B} \left(\tilde{\phi}^{\mathrm{c}} \alpha \tilde{\mathbf{B}} \cdot \delta\mathbf{u}^{e} + \tilde{\phi}^{\mathrm{c}} \beta \mathbf{N}_{\mathrm{f}} \cdot \delta\mathbf{p}^{e} - \mathbf{m}^{\mathrm{T}} \cdot \mathbf{N}_{\mathrm{p}} \cdot \delta\boldsymbol{\Phi}^{\mathrm{p},e} - \mathbf{N}_{\mathrm{f}} \cdot \delta\boldsymbol{\phi}^{\mathrm{m},e} \right) \Bigg] \mathrm{d}\Omega^{\mathrm{c},e} = 0, \quad \text{(C.22)}$$

$$\boldsymbol{\lambda}^{e\mathrm{T}} \int_{\Omega^{\mathrm{c},e}} \mathbf{N}_{f}^{\mathrm{T}} \left[\left(\tilde{\phi}^{\mathrm{c}}\, \alpha\, \tilde{\mathbf{B}} \cdot \dot{\mathbf{u}}^{e} + \tilde{\phi}^{\mathrm{c}}\, \beta\, \mathbf{N}_{\mathrm{f}} \cdot \dot{\mathbf{p}}^{e} - \mathbf{m}^{\mathrm{T}} \cdot \mathbf{N}_{\mathrm{p}} \cdot \dot{\boldsymbol{\Phi}}^{\mathrm{p},e} - \mathbf{N}_{\mathrm{f}} \cdot \dot{\boldsymbol{\phi}}^{\mathrm{m},e} \right) + \tilde{\phi}^{\mathrm{f}} \left(\alpha \tilde{\mathbf{B}} \cdot \dot{\mathbf{u}}^{e} + \beta \mathbf{N}_{\mathrm{f}} \cdot \dot{\mathbf{p}}^{e} \right) \right] \mathrm{d}\Omega^{\mathrm{c},e} + \boldsymbol{\lambda}^{e\mathrm{T}} \int_{\Omega^{\mathrm{c},e}} \mathbf{B}_{\mathrm{f}}^{\mathrm{T}} \left(\frac{\kappa}{\mu} \mathbf{B}_{\mathrm{f}} \cdot \tilde{p} + \frac{\kappa}{\mu} \mathbf{B}_{\mathrm{f}} \cdot \delta\mathbf{p}^{e} \right) \mathrm{d}\Omega^{\mathrm{c},e} = 0, \quad \text{(C.23)}$$

$$\boldsymbol{\Lambda}^{e\mathrm{T}} \int_{\Omega^{\mathrm{c},e}} \mathbf{N}_{\mathrm{p}}^{\mathrm{T}} \Bigg[\mathbf{N}_{\mathrm{p}} \cdot \dot{\boldsymbol{\Phi}}^{\mathrm{p},e} + \{\boldsymbol{\Phi}^{\mathrm{p}}\} \left(\alpha\, \tilde{\mathbf{B}} \cdot \dot{\mathbf{u}}^{e} + \beta\, \mathbf{N}_{\mathrm{f}} \cdot \dot{\mathbf{p}}^{e} \right) - \left(\frac{M^{\mathrm{p}}}{M^{\mathrm{m}}} \left(\frac{1}{2} k_0^{\mathrm{f}} \mathbf{m} + k_1^{\mathrm{f}} \{\tilde{\mathbf{T}}^{\mathrm{p}}\} \right) \frac{\tilde{\phi}^{\mathrm{m}}}{\tilde{\phi}^{\mathrm{f}}} - k_0^{\mathrm{d}} \mathbf{N}_{\mathrm{p}} \cdot \boldsymbol{\Phi}^{\mathrm{p},e} \right) - \left(\frac{M^{\mathrm{p}}}{M^{\mathrm{m}}} k_1^{\mathrm{f}} \left(\frac{\{\partial \mathbf{T}^{\mathrm{p}}\}}{\{\partial \boldsymbol{\Phi}^{\mathrm{p}}\}} \cdot \mathbf{N}^{\mathrm{p}} \cdot \delta\boldsymbol{\Phi}^{\mathrm{p},e} + \frac{\partial \{\mathbf{T}^{\mathrm{p}}\}}{\partial \{\mathbf{E}\}} \cdot \mathbf{F}^{\mathrm{m}} \cdot \mathbf{B} \cdot \delta\mathbf{u}^{e} + \frac{\partial \{\mathbf{T}^{\mathrm{p}}\}}{\partial \{\dot{\mathbf{E}}\}} \cdot \mathbf{F}^{\mathrm{m}} \cdot \mathbf{B} \cdot \dot{\mathbf{u}}^{e} + \{\{\mathbf{T}^{\mathrm{p}}\}\} \cdot \mathbf{G} \cdot \delta\mathbf{u} \right) \frac{\tilde{\phi}^{\mathrm{m}}}{\tilde{\phi}^{\mathrm{f}}} \right) - \left(\frac{M^{\mathrm{p}}}{M^{\mathrm{m}}} \left(\frac{1}{2} k_0^{\mathrm{f}} \mathbf{m} + k_1^{\mathrm{f}} \{\tilde{\mathbf{T}}^{\mathrm{p}}\} \right) \frac{\mathbf{N}_{\mathrm{p}} \cdot \delta\boldsymbol{\phi}^{\mathrm{m},e}}{\tilde{\phi}^{\mathrm{f}}} - k_0^{\mathrm{d}}\, \mathbf{N}_{\mathrm{p}} \cdot \delta\boldsymbol{\Phi}^{\mathrm{p},e} \right) - \frac{M^{\mathrm{p}}}{M^{\mathrm{m}}} \left(\frac{1}{2} k_0^{\mathrm{f}} \mathbf{m} + k_1^{\mathrm{f}} \{\tilde{\mathbf{T}}^{\mathrm{p}}\} \right) \frac{-\tilde{\phi}^{\mathrm{m}}}{\tilde{\phi}^{\mathrm{f}^2}} \cdot \left(\tilde{\phi}^{\mathrm{c}}\, \alpha\, \tilde{\mathbf{B}} \cdot \delta\mathbf{u}^{e} + \tilde{\phi}^{\mathrm{c}}\, \beta\, \mathbf{N}_{\mathrm{f}} \cdot \delta\mathbf{p}^{e} - \mathbf{m}^{\mathrm{T}} \cdot \mathbf{N}_{\mathrm{p}} \cdot \delta\boldsymbol{\Phi}^{\mathrm{p},e} - \mathbf{N}_{\mathrm{f}} \cdot \delta\boldsymbol{\phi}^{\mathrm{m},e} \right) \Bigg] \mathrm{d}\Omega^{\mathrm{c},e} = 0. \quad \text{(C.24)}$$

DOI: 10.1002/nme

In the preceding equations, $\mathbf{m}^{\mathrm{T}} = \{1\ 1\ 0\}$, and the matrix $\mathbf{M}_{\mathrm{p}}$ is defined such that in Voigt notation one can write $\{\mathbf{A}_\sigma\} = \mathbf{M}_{\mathrm{p}} \cdot \{\mathbf{A}\}$, where $\{\mathbf{A}_\sigma\}$ and $\{\mathbf{A}\}$ are vector forms of symmetric tensors $\mathbf{A}_\sigma$ and $\mathbf{A}$, respectively. As a result, the matrix $\mathbf{M}_{\mathrm{p}}$ takes the following form [48]:

$$\mathbf{M}_{\mathrm{p}} = \begin{bmatrix} P_{11}^2 & P_{12}^2 & P_{11}P_{12} \\ P_{12}^2 & P_{22}^2 & P_{22}P_{12} \\ 2P_{11}P_{12} & 2P_{22}P_{12} & P_{12}^2 + P_{11}P_{22} \end{bmatrix}. \tag{C.25}$$

Also, the cortex's stiffness matrix $\{\mathbf{S}_\sigma\}$ can be calculated by using its elastic matrix $\{\mathbf{C}_\sigma\}$ by $\{\mathbf{S}_\sigma\} = \mathbf{M}_{\mathrm{p}}^{\mathrm{T}} \cdot \{\mathbf{C}_\sigma\} \cdot \mathbf{M}_{\mathrm{p}}$. Furthermore, the notation $\{\mathbf{C}\}$ is used to define the fourth-order constitutive matrix $\mathbf{C}$ as a second-order matrix in Voigt notation.

APPENDIX D: COMPONENTS OF FINAL EQUATION (46)

The components of Equation (46) are given by the following:

$$\mathbf{F}^{u^{\mathrm{s}},e} = \int_{\Omega^{\mathrm{s}}} \mathbf{B}^{\mathrm{s}\mathrm{T}} \cdot \{\tilde{\mathbf{T}}^{\mathrm{s}}\}\, \mathrm{d}\Omega^{\mathrm{s}} - \int_{\Omega^{\mathrm{c}}} \mathbf{N}^{\mathrm{s}\mathrm{T}} \cdot \tilde{\mathbf{t}}_{\mathrm{a}}\, \mathrm{d}\Omega^{\mathrm{c}}, \tag{D.1}$$

$$\mathbf{F}^{u,e} = \int_{\Omega^{\mathrm{c}}} \left[\mathbf{B}^{\mathrm{T}} \left(\{\tilde{\mathbf{T}}^{\mathrm{c}}\} + \{\tilde{\mathbf{T}}^{\mathrm{p}}\}\right) - \tilde{\mathbf{B}}^{\mathrm{T}} \cdot p + \mathbf{N}^{\mathrm{T}} \cdot \tilde{\mathbf{t}}_{\mathrm{a}}\right] \mathrm{d}\Omega^{\mathrm{c}} + \int_{\Gamma^{\mathrm{c}}} \mathbf{B}^{\mathrm{T}} \mathbf{M}_{\mathrm{p}}^{\mathrm{T}} \cdot \{\tilde{\mathbf{T}}_\sigma\} \mathrm{d}\Gamma^{\mathrm{c}}, \tag{D.2}$$

$$\mathbf{F}^{\mathrm{f},e} = \int_{\Omega^{\mathrm{c}}} \mathbf{B}_{\mathrm{f}}{}^{\mathrm{T}} \left[\frac{\kappa}{\mu} \mathbf{B}_{\mathrm{f}} \cdot \mathbf{p}^e + \left(\frac{\tilde{\phi}^{\mathrm{m}}}{\tilde{\phi}^{\mathrm{f}}} \frac{\kappa}{\mu} \mathbf{B}_{\mathrm{f}} \cdot \mathbf{p}^e + D\ \mathbf{B}_{\mathrm{f}} \cdot \boldsymbol{\phi}^{\mathrm{m},e} - \frac{\tilde{\phi}^{\mathrm{m}}}{\tilde{\phi}^{\mathrm{f}}} D\ \nabla \tilde{\phi}^{\mathrm{f}}\right)\right] \mathrm{d}\Omega^{\mathrm{c}}, \tag{D.3}$$

$$\mathbf{F}^{\mathrm{m},e} = \int_{\Omega^{\mathrm{c}}} \mathbf{B}_{\mathrm{f}}^{\mathrm{T}} \cdot \frac{\kappa}{\mu} \mathbf{B}_{\mathrm{f}} \cdot \mathbf{p}^e\, \mathrm{d}\Omega^{\mathrm{c}}, \tag{D.4}$$

$$\mathbf{F}^{\mathrm{p},e} = -\int_{\Omega^{\mathrm{c}}} \mathbf{N}_{\mathrm{p}}^{\mathrm{T}} \cdot \left(\frac{M^{\mathrm{p}}}{M^{\mathrm{m}}} \left(\frac{1}{2} k_0^{\mathrm{f}} \mathbf{m} + k_1^{\mathrm{f}} \{\tilde{\mathbf{T}}^{\mathrm{p}}\}\right) \frac{\tilde{\phi}^{\mathrm{m}}}{\tilde{\phi}^{\mathrm{f}}} - k_0^{\mathrm{d}} \mathbf{N}_{\mathrm{p}} \cdot \boldsymbol{\Phi}^{\mathrm{p},e}\right) \mathrm{d}\Omega^{\mathrm{c}} \tag{D.5}$$

and

$$\mathbf{K}^{\mathrm{ss},e} = \int_{\Omega^{\mathrm{s}}} \mathbf{B}^{\mathrm{s}\mathrm{T}} \cdot \{\mathbf{C}^{\mathrm{s}}\} \cdot \mathbf{B}^{\mathrm{s}}\, \mathrm{d}\Omega^{\mathrm{s}} + \int_{\Omega^{\mathrm{c}}} \mathbf{N}^{\mathrm{s}\mathrm{T}} \cdot \mathbf{K}_{\mathrm{a}} \cdot \mathbf{N}^{\mathrm{s}}\, \mathrm{d}\Omega^{\mathrm{c}} \tag{D.6}$$

$$\mathbf{K}^{\mathrm{s}u,e} = -\int_{\Omega^{\mathrm{c}}} \mathbf{N}^{\mathrm{s}\mathrm{T}} \cdot \mathbf{K}_{\mathrm{a}} \cdot \mathbf{N}\, \mathrm{d}\Omega^{\mathrm{c}}, \tag{D.7}$$

$$\mathbf{K}^{u\mathrm{s},e} = -\int_{\Omega^{\mathrm{c}}} \mathbf{N}^{\mathrm{T}} \cdot \mathbf{K}_{\mathrm{a}} \cdot \mathbf{N}^{\mathrm{s}}\, \mathrm{d}\Omega^{\mathrm{c}}, \tag{D.8}$$

$$\begin{aligned} \mathbf{K}^{uu,e} = & \int_{\Omega^{\mathrm{c}}} \mathbf{B}^{\mathrm{T}} \cdot \left(\{\mathbf{C}^{\mathrm{c}}\} \cdot \mathbf{B} + \{\{\mathbf{T}^{\mathrm{c}}\}\} \cdot \mathbf{G} + \frac{\partial \{\mathbf{T}^{\mathrm{p}}\}}{\partial \{\mathbf{E}\}} \cdot \mathbf{F}^{\mathrm{m}} \cdot \mathbf{B} + \{\{\mathbf{T}^{\mathrm{p}}\}\} \cdot \mathbf{G}\right) \mathrm{d}\Omega^{\mathrm{c}} \\ & + \int_{\Omega^{\mathrm{c}}} \mathbf{N}^{\mathrm{T}} \cdot \mathbf{K}_{\mathrm{a}} \cdot \mathbf{N}\, \mathrm{d}\Omega^{\mathrm{c}} \\ & + \int_{\Gamma^{\mathrm{c}}} \left(\mathbf{B}^{\mathrm{T}} \cdot \mathbf{M}_{\mathrm{p}}^{\mathrm{T}} \cdot \{\mathbf{S}^{\mathrm{s}}\} \cdot \mathbf{M}_{\mathrm{p}} \cdot \mathbf{B} + \mathbf{B}^{\mathrm{T}} \cdot \mathbf{M}_{\mathrm{p}}^{\mathrm{T}} \cdot \{\{\mathbf{T}_\sigma\}\} \cdot \mathbf{M}_{\mathrm{p}} \cdot \mathbf{G}\right) \mathrm{d}\Gamma^{\mathrm{c}}, \end{aligned} \tag{D.9}$$

$$\mathbf{K}^{u\mathrm{f},e} = -\int_{\Omega^{\mathrm{c}}} \tilde{\mathbf{B}}^{\mathrm{T}} \cdot \frac{1-2\nu}{1-\nu} \mathbf{N}_{\mathrm{f}}\, \mathrm{d}\Omega^{\mathrm{c}}, \tag{D.10}$$

$$\mathbf{K}^{u\mathrm{p},e} = \int_{\Omega^{\mathrm{c}}} \mathbf{B}^{\mathrm{T}} \cdot \frac{\{\partial \mathbf{T}^{\mathrm{p}}\}}{\{\partial \boldsymbol{\Phi}^{\mathrm{p}}\}} \cdot \mathbf{N}_{\mathrm{p}}\, \mathrm{d}\Omega^{\mathrm{c}}, \tag{D.11}$$

DOI: 10.1002/nme

$$\mathbf{K}^{fu,e} = \int_{\Omega^c} \mathbf{B}_f^T \frac{\tilde{\phi}^m}{\tilde{\phi}^f} \left(-\frac{1}{\tilde{\phi}^f} \frac{\kappa}{\mu} \mathbf{B}_f \cdot \mathbf{p}^e + \frac{1}{\tilde{\phi}^f} D \nabla \tilde{\phi}^f \right) \cdot \tilde{\phi}^c \alpha \tilde{\mathbf{B}} \, d\Omega^c - \int_{\Omega^c} \mathbf{B}_f^T \frac{\tilde{\phi}^m}{\tilde{\phi}^f} D \mathbf{B} \left(\tilde{\phi}^c \alpha \tilde{\mathbf{B}} \right) d\Omega^c, \tag{D.12}$$

$$\mathbf{K}^{ff,e} = \int_{\Omega^c} \mathbf{B}_f^T \left(1 + \frac{\tilde{\phi}^m}{\tilde{\phi}^f} \right) \frac{\kappa}{\mu} \mathbf{B}_f \, d\Omega^c + \int_{\Omega^c} \mathbf{B}_f^T \frac{\tilde{\phi}^m}{\tilde{\phi}^f} \left(-\frac{1}{\tilde{\phi}^f} \frac{\kappa}{\mu} \mathbf{B}_f \cdot \mathbf{p}^e + \frac{1}{\tilde{\phi}^f} D \nabla \tilde{\phi}^f \right) \cdot \tilde{\phi}^c \beta \mathbf{N}_f \, d\Omega^c - \int_{\Omega^c} \mathbf{B}_f^T \frac{\tilde{\phi}^m}{\tilde{\phi}^f} D \mathbf{B} \left(\tilde{\phi}^c \beta \mathbf{N}_f \right) d\Omega^c, \tag{D.13}$$

$$\mathbf{K}^{fm,e} = \int_{\Omega^c} \mathbf{B}_f^T \left(\frac{1}{\tilde{\phi}^f} \frac{\kappa}{\mu} \mathbf{B}_f \cdot \mathbf{p}^e \cdot \mathbf{N}_f + D \mathbf{B}_f - \frac{1}{\tilde{\phi}^f} D \nabla \tilde{\phi}^f \cdot \mathbf{N}_f \right) d\Omega^c + \int_{\Omega^c} \mathbf{B}_f^T \frac{\tilde{\phi}^m}{\tilde{\phi}^f} \left(-\frac{1}{\tilde{\phi}^f} \frac{\kappa}{\mu} \mathbf{B}_f \cdot \mathbf{p}^e + \frac{1}{\tilde{\phi}^f} D \nabla \tilde{\phi}^f \right) \cdot (-\mathbf{N}_f) \, d\Omega^c - \int_{\Omega^c} \mathbf{B}_f^T \frac{\tilde{\phi}^m}{\tilde{\phi}^f} D \mathbf{B} (-\mathbf{N}_f) \, d\Omega^c, \tag{D.14}$$

$$\mathbf{K}^{fp,e} = \int_{\Omega^c} \mathbf{B}_f^T \frac{\tilde{\phi}^m}{\tilde{\phi}^f} \left(-\frac{1}{\tilde{\phi}^f} \frac{\kappa}{\mu} \mathbf{B}_f \cdot \mathbf{p}^e + \frac{1}{\tilde{\phi}^f} D \nabla \tilde{\phi}^f \right) \cdot \left(-\mathbf{m}^T \cdot \mathbf{N}_p \right) d\Omega^c - \int_{\Omega^c} \mathbf{B}_f^T \frac{\tilde{\phi}^m}{\tilde{\phi}^f} D \mathbf{B} \left(-\mathbf{m}^T \cdot \mathbf{N}_p \right) d\Omega^c, \tag{D.15}$$

$$\mathbf{K}^{mf,e} = \int_{\Omega^c} \mathbf{B}_f^T \cdot \left(\frac{\kappa}{\mu} \mathbf{B}_f \right) d\Omega^c, \tag{D.16}$$

$$\mathbf{K}^{pu,e} = -\int_{\Omega^c} \mathbf{N}_p^T \left(\frac{M^p}{M^m} k_1^f \left(\frac{\partial \{\mathbf{T}^p\}}{\partial \{\mathbf{E}\}} \cdot \mathbf{F}^m \cdot \mathbf{B} + \{\{\mathbf{T}^p\}\} \cdot \mathbf{G} \right) \frac{\tilde{\phi}^m}{\tilde{\phi}^f} \right) d\Omega^c - \int_{\Omega^c} \mathbf{N}_p^T \frac{M^p}{M^m} \left(\frac{1}{2} k_0^f \mathbf{m} + k_1^f \{\tilde{\mathbf{T}}^p\} \right) \frac{-\tilde{\phi}^m}{\tilde{\phi}^{f2}} \cdot \left(\tilde{\phi}^c \alpha \tilde{\mathbf{B}} \right) d\Omega^c, \tag{D.17}$$

$$\mathbf{K}^{pf,e} = -\int_{\Omega^c} \mathbf{N}_p^T \frac{M^p}{M^m} \left(\frac{1}{2} k_0^f \mathbf{m} + k_1^f \{\tilde{\mathbf{T}}^p\} \right) \frac{-\tilde{\phi}^m}{\tilde{\phi}^{f2}} \cdot \tilde{\phi}^c \beta \mathbf{N}_f \, d\Omega^c, \tag{D.18}$$

$$\mathbf{K}^{pm,e} = -\int_{\Omega^c} \mathbf{N}_p^T \left(\frac{M^p}{M^m} \left(\frac{1}{2} k_0^f \mathbf{m} + k_1^f \{\tilde{\mathbf{T}}^p\} \right) \frac{1}{\tilde{\phi}^f} \mathbf{N}_p \right) d\Omega^c - \int_{\Omega^c} \mathbf{N}_p^T \frac{M^p}{M^m} \left(\frac{1}{2} k_0^f \mathbf{m} + k_1^f \{\tilde{\mathbf{T}}^p\} \right) \frac{-\tilde{\phi}^m}{\tilde{\phi}^{f2}} \cdot (-\mathbf{N}_f) \, d\Omega^c, \tag{D.19}$$

$$\mathbf{K}^{pp,e} = -\int_{\Omega^c} \mathbf{N}_p^T \left[\left(\frac{M^p}{M^m} k_1^f \left(\frac{\{\partial \mathbf{T}^p\}}{\{\partial \mathbf{\Phi}^p\}} \cdot \mathbf{N}^p \right) \frac{\tilde{\phi}^m}{\tilde{\phi}^f} \right) - k_0^d \mathbf{N}_p \right] d\Omega^c - \int_{\Omega^c} \mathbf{N}_p^T \frac{M^p}{M^m} \left(\frac{1}{2} k_0^f \mathbf{m} + k_1^f \{\tilde{\mathbf{T}}^p\} \right) \frac{-\tilde{\phi}^m}{\tilde{\phi}^{f2}} \cdot \left(-\mathbf{m}^T \cdot \mathbf{N}_p \right) d\Omega^c, \tag{D.20}$$

$$\mathbf{C}^{uu,e} = \int_{\Omega^c} \mathbf{B}^T \frac{\partial \{\mathbf{T}^p\}}{\partial \{\dot{\mathbf{E}}\}} \cdot \mathbf{F}^m \cdot \mathbf{B} \, d\Omega^c, \tag{D.21}$$

$$\mathbf{C}^{fu,e} = \int_{\Omega^c} \mathbf{N}_f{}^T \left[\alpha \tilde{\mathbf{B}} \right] d\Omega^c, \tag{D.22}$$

DOI: 10.1002/nme

and

$$\mathbf{C}^{\mathrm{ff},e} = \int_{\Omega^{\mathrm{c}}} \mathbf{N}_{\mathrm{f}}{}^{\mathrm{T}} \left[\beta \, \mathbf{N}_{\mathrm{f}} \right] \, \mathrm{d}\Omega^{\mathrm{c}}, \tag{D.23}$$

$$\mathbf{C}^{\mathrm{m}u,e} = \int_{\Omega^{\mathrm{c}}} \mathbf{N}_{\mathrm{f}}^{\mathrm{T}} \cdot \left(\phi^{\mathrm{c}} + \phi^{\mathrm{f}} \right) \, \alpha \, \tilde{\mathbf{B}} \, \mathrm{d}\Omega^{\mathrm{c}}, \tag{D.24}$$

$$\mathbf{C}^{\mathrm{mf},e} = \int_{\Omega^{\mathrm{c}}} \mathbf{N}_{\mathrm{f}}^{\mathrm{T}} \left(\phi^{\mathrm{c}} + \phi^{\mathrm{f}} \right) \, \beta \, \mathbf{N}_{\mathrm{f}} \, \mathrm{d}\Omega^{\mathrm{c}}, \tag{D.25}$$

$$\mathbf{C}^{\mathrm{mm},e} = \int_{\Omega^{\mathrm{c}}} \mathbf{N}_{\mathrm{f}}^{\mathrm{T}} \left(-\mathbf{N}_{\mathrm{f}} \right) \, \mathrm{d}\Omega^{\mathrm{c}}, \tag{D.26}$$

$$\mathbf{C}^{\mathrm{mp},e} = \int_{\Omega^{\mathrm{c}}} \mathbf{N}_{\mathrm{f}}^{\mathrm{T}} \left(-\mathbf{m}^{\mathrm{T}} \cdot \mathbf{N}_{\mathrm{p}} \right) \, \mathrm{d}\Omega^{\mathrm{c}}, \tag{D.27}$$

$$\mathbf{C}^{\mathrm{p}u,e} = \int_{\Omega^{\mathrm{c}}} \left[\mathbf{N}_{\mathrm{p}}^{\mathrm{T}} \cdot \{ \mathbf{\Phi}^{\mathrm{p}} \} \, \alpha \, \tilde{\mathbf{B}} \cdot \dot{\mathbf{u}}^{e} - \mathbf{N}_{\mathrm{p}}^{\mathrm{T}} \cdot \frac{M^{\mathrm{p}}}{M^{\mathrm{m}}} k_1^{f} \left(\frac{\partial \{ \mathbf{T}^{\mathrm{p}} \}}{\partial \{ \dot{\mathbf{E}} \}} \cdot \mathbf{F}^{\mathrm{m}} \cdot \mathbf{B} \right) \frac{\tilde{\phi}^{\mathrm{m}}}{\tilde{\phi}^{\mathrm{f}}} \right] \, \mathrm{d}\Omega^{\mathrm{c}}, \tag{D.28}$$

$$\mathbf{C}^{\mathrm{pf},e} = \int_{\Omega^{\mathrm{c}}} \mathbf{N}_{\mathrm{p}}^{\mathrm{T}} \cdot \{ \mathbf{\Phi}^{\mathrm{p}} \} \, \beta \, \mathbf{N}_{\mathrm{f}} \, \mathrm{d}\Omega^{\mathrm{c}}, \tag{D.29}$$

$$\mathbf{C}^{\mathrm{pp},e} = \int_{\Omega^{\mathrm{c}}} \mathbf{N}_{\mathrm{p}}^{\mathrm{T}} \cdot \mathbf{N}_{\mathrm{p}} \, \mathrm{d}\Omega^{\mathrm{c}}. \tag{D.30}$$

ACKNOWLEDGEMENTS

FJV gratefully acknowledges the University of Colorado CRCW Seed Grant and NSF grant number CMMI-0900607 in support of this research.

REFERENCES

1. Baxter SC, Morales MO, Goldsmith EC. Adaptive changes in cardiac fibroblast morphology and collagen organization as a result of mechanical environment. *Cell Biochemistry and Biophysics* 2008; **51**:33–44.
2. Fernandez P, Bausch A. The compaction of gels by cells: a case of collective mechanical activity. *Integrative Biology* 2009; **1**:252–259.
3. Freyman TM, Yannas IV, Pek Y-S, Yokoo R, Gibson LJ. Fibroblast contraction of a collagen-gag matrix. *Biomaterials* 2001; **22**:2883–2891.
4. Ohsumi TK, Flaherty JE, Evans M, Barocas V. Three-dimensional simulation of anisotropic cell-driven collagen gel compaction. *Biomechanics and Modeling in Mechanobiology* 2008; **7**:53–62.
5. Wang J, Jia F, Gilbert T, Woo S. Cell orientation determines the alignment of cell-produced collagenous matrix. *Journal of Biomechanics* 2003; **36**(1):97–102.
6. Grinnel F, Lamke C. Reorganization of hydrated collagen lattices by human skin fibroblasts. *Journal of Cell Science* 1984; **66**:51–63.
7. Costa K, Lee E, Holmes J. Creating alignment and anisotropy and engineering heart tissue: role of boundary conditions in a model three-dimensional culture system. *Tissue Engineering* 2003; **9**(4):567–577.
8. Mohrdieck C, Wanner A, Wouter R, Roth A, Sackmann E, Spatz J, Arzt E. A theoretical description of elastic pillar substrates in biophysical experiments. *ChemPhysChem* 2005; **6**:1492–1498.
9. Bischofs IB, Klein F, Lehnert D, Bastmeyer M, Schwuartz US. Filamentous network mechanics and active contractility determine cell and tissue shape. *Biophysics Journal* 2008; **95**:3488–3496.
10. Nelson CM, Jean R, Tan J, Liu W, Snladeckl N, Spector A, Chen CS. Emergent patterns of growth controlled by multicellular form and mechanics. *Proceedings of the National Academy of Science* 2005; **102**(33):11594–11599.
11. Vernerey FJ, Greenwald E, Bryant S. Triphasic mixture model of cell-mediated enzymatic degradation of hydrogels. *Computer Methods in Biomechanics and Biomedical Engineering* 2011. DOI:10.1080/10255842.2011.585973.
12. Deshpande V, McMeeking R, Evans A. A bio-chemo-mechanical model for cell contractibility. *Proceedings of the National Academy of Science* 2006; **103**(38):14015–14020.
13. Deshpande V, Mrksich M, McMeeking R, Evans A. A bio-mechanical model for coupling cell contractility with focal adhesion formation. *Journal of the Mechanics and Physics of Solids* 2008; **56**:1484–1510.
14. Vernerey FJ, Farsad M. A constrained mixture approach to mechano-sensing and force generation in contractile cells. *Journal of the Mechanical Behavior of Biomedical Materials* 2011. DOI: 10.1016/j.jmbbm.2011.05.022.
15. Vernerey FJ, Farsad M. An Eulerian/XFEM formulation for the large deformation of cortical cell membrane. *Computer Methods in Biomechanics and Biomedical Engineering* 2011; **14**(5):433–445.
16. McGarry JP, Murphy BP, McHugh PE. Computational mechanics modelling of cell substrate contact during cyclic substrate deformation. *Journal of the Mechanics and Physics of Solids* 2005; **53**:2597–2637.

17. Qiua J, Tanga T, Zhanga M, Zhuang Z. 2-D finite element simulation of cell–substrate debonding during cyclic stretch. *Tsinghua Science and Technology* 2009; **14**(2):27–31.
18. Yamada H, Mouri N, Nobuhara S. Three-dimensional morphometry of single endothelial cells with substrate stretching and image-based finite element modeling. *EURASIP Journal on Advances in Signal Processing* 2010; **2010**:Article ID 616091, 10 pages.
19. Wong HC, Tang WC. Finite element analysis of the effects of focal adhesion mechanical properties and substrate stiffness on cell migration. *Journal of Biomechanics* 2011; **44**(6):1046–1050.
20. Dolbow J, Möes N, Belytschko T. An extended finite element method for modeling crack growth with frictional contact. *Computer Methods in Applied Mechanics and Engineering* 2001; **190**(51–52):6825–6846.
21. Möes N, Cloirec M, Cartraud P, Remacle JF. A computational approach to handle complex microstructure geometries. *Computer Methods in Applied Mechanics and Engineering* 2003; **192**:3163–3177.
22. Belytschko T, Parimi C, Möes N, Sukumar N, Usui S. Structured extended finite element methods for solids defined by implicit surfaces. *International Journal for Numerical Methods in Engineering* 2003; **56**(4):609–635.
23. Dzyubachyk O, van Cappellen WA, Essers J, Niessen WJ, Meijering E. Advanced level-set-based cell tracking in time-lapse fluorescence microscopy. *IEEE Transactions on Medical Imaging* 2010; **29**(3):825–867.
24. Duddu R, Bordas S, Chopp D, Moran B. A combined extended finite element and level set method for biofilm growth. *International Journal for Numerical Methods in Engineering* 2008; **74**:848–870.
25. Coughlin MF, Stamenovic D. A prestressed cable network model of the adherent cell cytoskeleton. *Biophysics Journal* 2003; **84**:1328–1336.
26. Deshpande VS, McMeeking RM, Evans AG. A bio-chemo-mechanical model for cell contractility. *Proceedings of the National Academy of Science* 2006; **103**(38):14015–14020.
27. Walcott S, Sun SX. A mechanical model of actin stress fiber formation and substrate elasticity sensing in adherent cells. *Proceedings of the National Academy of Science* 2010; **107**(17):7757–7762.
28. Wang N, Butler JP, Ingber DE. Mechanotransduction across the cell surface and through the cytoskeleton. *Science* 1993; **260**:1124–1127.
29. Choquet D, Felsenfeld DF, Sheetz MP. Extracellular matrix rigidity causes strengthening of integrin–cytoskeletal linkages. *Cell* 1997; **88**:39–48.
30. Lecuit T, Lenne PF. Cell surface mechanics and the control of cell shape, tissue patterns and morphogenesis. *Nature Reviews Molecular Cell Biology* 2007; **8**:633–644.
31. Karcher H, Lammerding J, Huang H, Lee RT, Kamm RD, Kaazempur-Mofrad MR. A three-dimensional viscoelastic model for cell deformation with experimental verification. *Biophysics Journal* 2003; **85**:3336–3349.
32. Unnikrishnan GU, Unnikrishnan VU. Constitutive material modeling of cell: a micromechanics approach. *Journal of Biomechanical Engineering* 2007; **129**:315–323.
33. Kumar S, Maxwell IZ, Heisterkamp A, Polte TR, Lele TP, Salanga M, Mazur E, Ingber DE. Viscoelastic retraction of single living stress fibers and its impact on cell shape, cytoskeletal organization, and extracellular matrix mechanics. *Biophysics Journal* 2006; **85**:3762–3773.
34. Stachowiak MR, OShaughnessy B. Kinetics of stress fibers. *New Journal of Physics* 2008; **10**:1–26.
35. Paul R, Heil P, Spatz JP, Schwarz US. Propagation of mechanical stress through the actin cytoskeleton toward focal adhesions: model and experiment. *Biophysics Journal* 2008; **94**:1470–1482.
36. Gardel ML, Shin JH, MacKintosh FC, Mahadevan L, Matsudaira P, Weitz DA. Elastic behavior of cross-linked and bundled actin networks. *Science* 2004; **304**:1301–1305.
37. Carlson F, Wilkie D. *Muscle Physiology*. Prentice Hall: Upper Saddle River, 1974.
38. Hill AV. The heat of shortening and the dynamic constant of muscles. *Proceedings of the Royal Society B* 1938; **126**:136–195.
39. Yeung T, George PC, Flanagan LA, Marge B, Ortiz M, Funaki M, Zahir N, Ming W, Weaver V, Janmey PA. Effects of substrate stiffness on cell morphology, cytoskeletal structure, and adhesion. *Cell Motility and the Cytoskeleton* 2005; **60**:24–34.
40. Engler AJ, Sen S, Sweeney HL, Discher DE. Matrix elasticity directs stem cell lineage specification. *Cell* 2006; **26**:687–689.
41. Discher DE, Janmey P, li Wang Y. Tissue cells feel and respond to the stiffness of their substrate. *Science* 2005; **310**:1139–1143.
42. Deshpande VS, Mrksichb M, McMeekingc RM, Evans AG. A bio-mechanical model for coupling cell contractility with focal adhesion formation. *Journal of the Mechanics and Physics of Solids* 2008; **56**:1484–1510.
43. Sethian JA. *Level Set Methods and Fast Marching Methods: Evolving Interfaces in Computational Geometry, Fluid Mechanics, Computer Vision, and Material Science*. Cambridge University Press: Cambridge, UK, 1999.
44. Sussman M, Almgren A, Bell JB, Colella P, Howell LH, Welcome ML. An adaptive level set approach for incompressible two-phase flows. *Journal of Computational Physics* 1999; **148**(1):81–124.
45. Sussman M, Fatemi E. An efficient interface preserving level set redistancing algorithm and its application to interfacial incompressible fluid flow. *Journal of Scientific Computing* 1999; **20**(4):1165–1191.
46. Hettich T, Hund A, Ramm E. Modeling of failure in composites by X-FEM and level sets within a multiscale framework. *Computer Methods in Applied Mechanics and Engineering* 2008; **197**:414–424.
47. Belytschko T, Gracie R. On XFEM applications to dislocations and interfaces. *International Journal of Plasticity* 2007; **23**(10–11):1721–1738.

DOI: 10.1002/nme

48. Yvonnet J, Quang HL, He QC. An XFEM/level set approach to modelling surface/interface effects and to computing the size-dependent effective properties of nanocomposites. *Computational Mechanics* 2008; **42**:119–131.
49. Farsad M, Vernerey FJ, Park HS. An extended finite element/level set method to study surface effects on the mechanical behavior and properties of nanomaterials. *International Journal for Numerical Methods in Engineering* 2010; **84**(12):1466–1489.
50. Mohammadi S. *Extended Finite Element Method*. Blackwell: Hoboken, 2008.
51. Möes N, Dolbow J, Belytschko. A finite element method for crack growth without remeshing. *International Journal for Numerical Methods in Engineering* 1999; **46**(1):131–150.
52. Belytschko T, Liu WK, Moran B. *Nonlinear Finite Elements for Continua and Structures*. John Wiley & Sons LTD: Hoboken, 2006.
53. Ateshian G, Likhitpanichkul M, Hung C. A mixture theory analysis for passive transport in osmotic loading of cells. *Journal of Biomechanics* 2006; **39**:464–475.
54. Rubinstein B, Jacobson K, Mogilner A. Multiscale two-dimensional modeling of a motile simple-shaped cell. *Multiscale Modeling & Simulation* 2005; **3**(2):413–439.
55. Guilak F, Mow V. The mechanical environment of the chondrocyte: a biphasic finite element model of cell–matrix interactions in articular cartilage. *Journal of Biomechanics* 2000; **33**:1663–1673.
56. White GE, Fujiwara K. Expression and intracellular distribution of stress fibers in aortic endothelium. *The Journal of Cell Biology* 1986; **103**:63–70.
57. Tsuda Y, Yasutake H, Ishijima A, Yanagida T. Torsional rigidity of single actin filaments and actin–actin bond breaking force under torsion measured directly by in vitro micromanipulation. *Proceedings of the National Academy of Science* 1996; **93**:12937–12942.
58. Schatzman M. *Numerical Analysis: A Mathematical Introduction*. Clarendon Press: Oxford, UK, 2002.
59. Vernerey FJ, *et al.* A micromorphic model for the multiple scale failure of heterogeneous materials. *Journal of the Mechanics and Physics of Solids* 2008; **56**(4):1320–1347.
60. Bray M, Sheehy SP, Parker KK. Sarcomere alignment is regulated by myocyte shape. *Cell Motility and the Cytoskeleton* 2008; **65**:641–651.
61. Parker KK, Tan J, Chen CS, Tung L. Myofibrillar architecture in engineered cardiac myocytes. *Circulation Research* 2008; **103**:340–342. DOI: 10.1161/CIRCRESAHA.108.182469.
62. Geisse NA, Sheehy SP, Parker KK. Control of myocyte remodeling in vitro with engineered substrates. *In Vitro Cellular & Developmental Biology—Animal* 2009; **45**:343–350.
63. Bray MP, Adams WJ, Geisse NA, Feinberg AW, Sheehy SP, Parker KK. Nuclear morphology and deformation in engineered cardiac myocytes and tissues. *Biomaterials* 2010; **31**:5143–5150.
64. Engler AJ, Carag-Krieger C, Johnson CP, Raab M, Tang HY, Speicher DW, Sanger JW, Sanger JM, Discher DE. Embryonic cardiomyocytes beat best on a matrix with heart-like elasticity: scar-like rigidity inhibits beating. *Journal of Cell Science* 2008; **121**:3794–3802.
65. Sunyer R, Trepat X, Fredberg JJ, Farre R, Navajas D. The temperature dependence of cell mechanics measured by atomic force microscopy. *Physical Biology* 2009; **6**:025009.
66. Wang HB, Dembo M, Wang Y. Substrate flexibility regulates growth and apoptosis of normal but not transformed cells. *American Journal of Physiology—Cell Physiology* 2000; **279**:C1345–C1350.
67. Solon J, Levental I, Sengupta K, Georges PC, Janmey PA. Fibroblast adaptation and stiffness matching to soft elastic substrates. *Biophysical Journal* 2007; **93**:4453–4461.
68. Guo W, Frey M, Burnham N, Wang Y. Substrate rigidity regulates the formation and maintenance of tissues. *Biophysical Journal* 2006; **90**:2213–2220.
69. Levental I, Georges P, Janmey P. Soft biological materials and their impact on cell function. *Soft Matter* 2006; **2**:1–9.
70. Bischofs IB, Schwarz US. Cell organization in soft media due to active mechanosensing. *Proceedings of the National Academy of Science* 2003; **100**(16):9274–9279.